RESEARCH ARTICLE

Aerofoil Trailing-edge Noise Prediction Models for Wind Turbine Applications

Alex Siu Hong Lau[1], Jae Wook Kim[1], Jeremy Hurault[2], Tomas Vronsky[2] and Phillip Joseph[3]

[1]Aerodynamics and Flight Mechanics Research Group, Aeronautics and Astronautics, University of Southampton, SO17 1BJ, UK
[2]Vestas, Blade Technology Centre, West Medina Mills, Stag Lane, Newport, Isle of Wight, PO30 5TR, UK
[3]Institute of Sound and Vibration Research, University of Southampton, SO17 1BJ, UK

ABSTRACT

This paper proposes a modified TNO model for the prediction of aerofoil trailing-edge noise for wind turbine applications. The capabilities of the current modified model and four variants of the TNO model are analysed through a comprehensive study which includes ten aerofoils and involves two different wind tunnels. Some of these aerofoils are used on modern large wind turbines. For the test cases considered, the Reynolds numbers are between 1.13 and 3.41 million, and the effective angles of attack are between -2.2° and 13.58°. The merit of a model is assessed by comparing two aspects of the numerically-predicted and the experimentally-measured sound pressure level spectra. The first aspect is the sound pressure level difference between two different aerofoils at similar lift coefficients within a certain frequency range (referred to as the delta noise). The second is the closeness of the predicted and measured sound pressure level spectra of the aerofoils in various flow configurations. From the baseline model, the current modified model is developed by deriving new formulations for the computation of the wall pressure fluctuation spectrum. This is achieved by using the approximate ratio of the normal Reynolds stress components for an anisotropic flow over a flat plate to estimate the vertical Reynolds stress component, and by introducing new stretching factors in the streamwise, vertical and spanwise directions to take the effects of turbulent flow anisotropy into account. Compared to the four TNO model variants tested, the current modified model has strong delta noise prediction ability, and is able to predict sound pressure level spectra which are more consistent and closer to measurements for the vast majority of aerofoils and flow conditions tested in the two wind tunnels.

KEYWORDS

Wind turbine; Aerofoil trailing-edge noise; Noise prediction model

Correspondence

Aerodynamics and Flight Mechanics Research Group, Aeronautics and Astronautics, University of Southampton, SO17 1BJ, UK.
E-mail: Alex.Lau@soton.ac.uk

Received . . .

1. INTRODUCTION

Wind power is an important renewable energy source in combating climate change. One major obstacle in the spread of onshore wind farms is noise [1]. For a modern wind turbine, most of the emitted noise is aerodynamically-generated

by the relative motion of air around its structures. A major contribution of wind turbine aerodynamic noise is trailing-edge (TE) noise, which is generated by the convecting turbulent eddies within the blade boundary-layer (BL) scattered into sound over the trailing-edge region of the blade. The angle of attack associated with TE noise is low to moderate such that flow separation over a large portion of the aerofoil chord has not occurred. For wind turbine blades, due to the increasing resultant flow velocity and the decreasing effective angle of attack from root to tip, lower-frequency noise (up to a few hundreds Hz) associated with larger eddies or separated flow could be dominant in the inboard section of a blade, while higher-frequency TE noise is emitted mainly from the outboard section. This spanwise variation of emitted noise frequency [2] depends on the size of the wind turbine, the blade geometry and the flow conditions. The current paper aims to develop an efficient and accurate TE noise prediction method, which can be used for wind turbine aerofoil and blade aeroacoustic performance estimation and optimisation.

A significant difficulty faced by the wind-energy industry in TE noise prediction arises from the high Reynolds numbers (Re) of the flow in the vicinity of a modern wind turbine blade tip, which are in the order of several millions. This renders advanced numerical methods [3, 4] based on three-dimensional computational fluid dynamics (3D CFD) or direct noise simulations impractical due to their long run time. Semi-empirical noise models [5, 6, 7, 8] can give predictions quickly. However, the accuracy of these models becomes questionable once the geometric and flow conditions deviate from the underlying empirical relations. Kraichnan [9] predicted the wall pressure fluctuations over a flat plate by considering the solutions of a Poisson equation, which was derived from the momentum equation for a turbulent BL over a smooth, stationary and rigid surface at low Mach number. From this Poisson equation, Blake [10] derived an expression for the wavenumber-frequency wall pressure fluctuation spectrum. Following the approach of Blake, Parchen [11] from the TNO Institute of Applied Physics in the Netherlands proposed a TE noise model which later became known as the TNO model. This model predicts the far-field TE noise from the estimated wavenumber-frequency wall pressure fluctuation spectrum by using a diffraction model for a semi-infinite plate, which is based on the works by Chandiramani [12], Brooks et al. [13] and Chase [14]. Therefore, in the original TNO model and many of its variants, the effects of finite chord and the presence of the leading-edge are neglected. So these models are only theoretically valid in the high-frequency limit when the aerofoil is considered non-compact. An alternative to the diffraction model is the far-field TE noise model proposed by Amiet [15, 16], which takes the effects of finite chord into account. Roger and Moreau [17] extended the Amiet far-field TE noise model to further include the effects of leading-edge back-scattering. It will be shown in the current paper that the use of the diffraction model for far-field TE noise prediction is reasonable for frequencies higher than 500Hz. However, its suitability for lower frequencies is unclear due to the lack of experimental measurement at those frequencies. Compared to semi-empirical models, the TNO model is fast to run and potentially more accurate and robust since more physics of the blade turbulent BL are taken into account. Some notable improvements to the TNO model, for example the introduction of more sophisticated modelling of the effects of flow anisotropy and the use of Reynolds-averaged Navier Stokes (RANS) simulations, have been suggested recently [18, 19, 20]. As a result, there exists a variety of TNO models. It will be shown in the current study that the level of agreement between experimental measurements and predictions by these models is highly dependent on the aerofoil geometry and the flow configurations. Hence there is a need to develop a more consistently accurate TNO model.

The current modified TNO model is developed by analysing four different TNO model variants, which are denoted as FB-Iso, FB-Aniso, MK-Iso and MK-Aniso. The former two are based on Bertagnolio et al. [20], and the latter two are based on Kamruzzaman et al. [19]. FB-Iso and MK-Iso employ isotropic flow assumptions to derive many constituent terms in the TNO formulations. The only difference between FB-Iso and MK-Iso is in the treatment of the computed mean energy dissipation rate. FB-Aniso and MK-Aniso use different anisotropic formulas to estimate the wall pressure fluctuation spectrum. The merit of a TNO model is assessed by comparing two aspects of the numerically-predicted and the experimentally-measured sound pressure level (SPL) spectra. The first aspect is the SPL difference between two different aerofoils at similar lift coefficients within a certain frequency range, referred to as the delta noise herein. The delta noise analysis will show the ability of a model to predict the change in SPL due to a change in the cross-sectional geometry at some blade spanwise location. The second aspect is the closeness of the predicted and measured SPL spectra for aerofoils

in various flow configurations. This is important when an accurate integrated SPL over a frequency range for an aerofoil is required.

The current comprehensive test and validation process employs experimental measurements for ten different aerofoils: seven in the delta noise analysis and seven in the SPL spectra closeness study. Hence four aerofoils are commonly used in both analyses. These experimental data were obtained in two different wind tunnels of very different designs. For all the current computations, the turbulent BL properties near the TE are estimated by coupling the BL prediction codes EDDYBL [21] and XFoil [22]. The EDDYBL Wilcox k-ω turbulence model is employed, and the boundary and initial conditions required are provided by a preliminary XFoil calculation, which is a panel method with viscous-inviscid interaction implemented.

The organisation of the paper is as follows. In section 2, the current modified model and the four TNO model variants tested are explained. Then, some predicted aerodynamic property profiles across the BL near the TE are compared to experimental measurements in section 3. After that in section 4, the delta noise prediction ability and the closeness of the predicted SPL spectra to measurements of the five TNO model variants are analysed and discussed. Finally, some conclusions are drawn in section 5.

2. THE FIVE TNO MODEL VARIANTS TESTED

In all variations of the TNO model, for a turbulent boundary-layer over a smooth, stationary and rigid aerofoil surface at a low Mach number (M), the wavenumber-frequency spectrum of the wall pressure fluctuations near the TE is given by [10, 11, 18, 19, 20]

$$\Phi_p(k_1, k_3, \omega) = 4\rho_0^2 \left[k_1^2/(k_1^2 + k_3^2)\right] \int_0^\infty \left\{ \Lambda_2 \left\langle u_2^2 \right\rangle \left(\partial U_1/\partial y_2\right)^2 \Phi_{22}\, \Phi_m\, e^{-2|\boldsymbol{k}|y_2} \right\} dy_2 \,, \tag{1}$$

where subscripts "1", "2" and "3" indicate the streamwise, vertical and spanwise directions respectively; y_2 is the vertical distance from the point on the surface where the BL properties required by the TNO model are evaluated, this evaluation point is at a x/c (the ratio of the streamwise distance from the leading-edge x to the aerofoil chord c) position of 0.995 if possible; ρ_0 is air density; ω is the angular frequency; k_1, k_2 and k_3 are the elements of the wavenumber vector such that $|\boldsymbol{k}| = \sqrt{{k_1}^2 + {k_2}^2 + {k_3}^2}$; $\Lambda_2 = \Lambda_2(y_2)$ is the vertical integral length scale of the vertical velocity fluctuations u_2; $\langle u_2^2 \rangle$ is the vertical Reynolds stress component; U_1 is the local mean streamwise velocity and $\partial U_1/\partial y_2$ is its gradient in the vertical direction; $\Phi_{22} = \Phi_{22}(k_1, k_3, k_e)$ is the normalised turbulence spectral tensor diagonal component (or spectrum) associated to u_2 after being integrated over k_2; k_e is the wavenumber of the energy-containing eddies; and $\Phi_m = \Phi_m(\omega - U_c\, k_1)$ is the moving-axis spectrum, which describes how the turbulent velocity spectrum is distorted by the evolution of eddies as they convect past the TE. In practice, the integration with respect to y_2 in equation 1 is performed from the wall to the edge of the BL, i.e. from $y_2 = 0$ to $y_2 = \delta$, where δ is the BL thickness.

An expression for the far-field pressure spectrum is derived by using a diffraction model for a semi-infinite plate [10, 11, 18, 19, 20], such that

$$S(\omega) = \frac{L}{4\pi r_o^2} \int_{-\infty}^{\infty} \frac{\omega}{c_0 k_1}\ \Phi_p(k_1, \omega)|_{k_3=0}\ dk_1, \tag{2}$$

where c_0 is the speed of sound; r_o is the observer distance; and L is the aerofoil span. This expression is only strictly valid in the high-frequency limit when the aerofoil is considered non-compact, i.e. the sound wavelength is smaller than the chord length c. It will be shown in section 4.2 that the use of equation 2 for far-field TE noise prediction is reasonable for frequencies higher than 500Hz. However, its suitability for lower frequencies is unclear due to the lack of experimental measurement at those frequencies. Note that all the spectra presented in this paper are one-sided but the spectrum described

by equation 2 is double-sided. Hence a factor of two is needed to be multiplied to equation 2. Equations 1 and 2 are commonly used by all the TNO model variants considered.

The moving-axis spectrum Φ_m can be approximated by a Dirac delta function if the turbulence is assumed to be frozen [20, 23], i.e.

$$\Phi_m = \delta(\omega - U_c k_1), \tag{3}$$

or by a Gaussian spectrum for non-frozen turbulence [18, 19], such that

$$\Phi_m = \frac{1}{\alpha_c \sqrt{\pi}} \exp\left[-\left(\frac{\omega - U_c k_1}{\alpha_c} \right)^2 \right], \tag{4}$$

where $\alpha_c = 0.05 U_c / \Lambda_2$ is the standard derivation of the Gaussian spectrum multiplied by $\sqrt{2}$. In both equations 3 and 4, U_c is the convective velocity and is approximated by $U_c = 0.7 U_1$. The current study found these two Φ_m formulations yield very similar results for the far-field SPL. Three examples are shown in Figure 1, which shows the far-field SPL spectra computed by FB-Iso TNO for a NACA64$_3$-418 aerofoil subjected to a freestream velocity U_∞ of 70m/s. The three flow configurations presented include a case with clean BL condition at an effective angle of attack α of 0°, and two cases with tripped BL condition at $\alpha = 0°$ and 3°. BL trip is applied at $x/c = 0.05$ on both sides of the aerofoil. It can be seen that for all the cases for frequencies higher than approximately 40Hz, the predicted spectra due to the two Φ_m formulations are nearly identical. The difference between these two Φ_m formulations is very small since BL properties are evaluated very close to the TE and so the assumption of frozen turbulence over this short distance to the TE is reasonable. The Dirac delta function is used in the current paper since the numerical integration with respect to k_1 from $-\infty$ to ∞ in the far-field noise computation can be avoided by using

$$\int_{-\infty}^{\infty} f(k_1)\delta(\omega - U_c k_1) dk_1 = \frac{1}{U_c} f\left(\frac{\omega}{U_c} \right),$$

where $f(\,)$ is any function. More details of the current aerodynamic calculation will be explained in section 3.

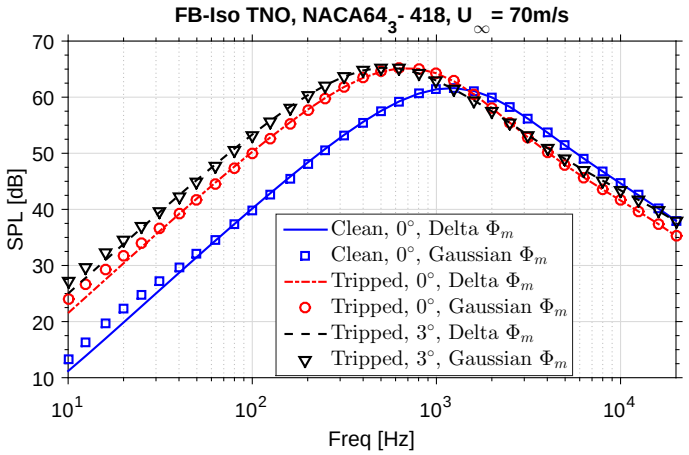

Figure 1. Predicted NACA64$_3$-418 aerofoil 1/3 octave SPL spectra by FB-Iso TNO with Φ_m given by equations 3 (Delta Φ_m) and 4 (Gaussian Φ_m)

2.1. Two Isotropic TNO Model Variants (FB-Iso and MK-Iso)

Both FB-Iso and MK-Iso assume isotropic turbulence. Hence Φ_{22} is given by

$$\Phi_{22} = \frac{4}{9\pi}\left(\frac{1}{k_e}\right)^2 \frac{(k_1/k_e)^2 + (k_3/k_e)^2}{[1+(k_1/k_e)^2+(k_3/k_e)^2]^{7/3}}. \tag{5}$$

Note that k_3 is set to zero in equation 5. An expression for k_e can be derived by comparing the asymptotic behaviour of the von Kármán spectrum and the Kolmogorov spectrum for the inertial subrange for isotropic turbulence [18, 24], such that

$$k_e = \left(\frac{1.5\times 27\sqrt{\pi}\ \Gamma(1/3)}{110\ \Gamma(5/6)}\right)^{3/2} \frac{\epsilon}{k_T^{3/2}} \approx 1.90\frac{\epsilon}{k_T^{3/2}}, \tag{6}$$

where Γ is the Gamma function, k_T is the turbulent kinetic energy and ϵ is the mean energy dissipation rate. It has been shown [18] that for an isotropic flow, k_e is also related to the vertical integral length scale Λ_2 by

$$k_e = \frac{\sqrt{\pi}\ \Gamma(5/6)}{\Gamma(1/3)\ \Lambda_2} \approx \frac{0.74}{\Lambda_2}. \tag{7}$$

From equations 6 and 7, an expression for the vertical integral length scale can be derived, such that

$$\Lambda_2 \approx 0.40\frac{k_T^{3/2}}{\epsilon}. \tag{8}$$

For isotropic turbulence, $\langle u_2^2\rangle$ is given by

$$\langle u_2^2\rangle = \frac{2}{3}k_T. \tag{9}$$

Equations 5, 6, 8 and 9 are used by the two isotropic TNO models to estimate Φ_{22}, k_e, Λ_2 and $\langle u_2^2\rangle$ respectively. k_T and ϵ are directly calculated by the current BL aerodynamic code.

The only difference between MK-Iso and FB-Iso arises from the treatment of the predicted mean energy dissipation rate ϵ of the turbulent BL near the TE. Kamruzzaman et al. [19] suggested a modification for ϵ near the wall, such that

$$\epsilon_{\text{mod}} = \left[c_5\frac{c_3}{c_1}(y^+)^{b(c_2-c_4)}\right]\epsilon, \tag{10}$$

where ϵ_{mod} is the modified mean energy dissipation rate, $y^+ = (y\,u_\tau)/\nu$ is the vertical distance above the wall non-dimensionalised by the friction velocity u_τ and the kinematic viscosity ν, $c_1 = 4.2$, $c_2 = 1.1$, $c_3 = 0.03$, $c_4 = 0.8$, $c_5 = 15$ and $b = 0.91$. Equation 10 reduces ϵ near the wall and is used by MK-Iso. FB-Iso uses the predicted ϵ directly.

2.2. Two Anisotropic TNO Model Variants (FB-Aniso and MK-Aniso)

Different anisotropy corrections are used in FB-Aniso and MK-Aniso models. Bertagnolio et al. [20] derived anisotropic expressions for Φ_{22} and Λ_2 by introducing three anisotropy stretching factors β_1, β_2, and β_3, which stretch the isotropic von Kármán spectrum in the streamwise, vertical and spanwise directions respectively. These stretching factors are given by

$$\beta_1 = 0.4; \tag{11}$$

$$\beta_2 = \gamma^{1/5}; \tag{12}$$

$$\beta_3 = (2\gamma)^{1/2}, \tag{13}$$

where γ is the non-dimensional mean pressure gradient and is defined as

$$\gamma = \frac{\delta}{u_\tau}\left[\frac{(\partial P/\partial y_1)^2}{\rho_0 \mu}\right]^{1/3}, \tag{14}$$

where P is the mean surface pressure and μ is the dynamic viscosity. Φ_{22} then becomes dependent on β_1 and β_3, such that

$$\Phi_{22\text{aniso}} = \frac{4}{9\pi}\left(\frac{1}{k_e}\right)^2 \beta_1\beta_3 \frac{(\beta_1 k_1/k_e)^2 + (\beta_3 k_3/k_e)^2}{[1+(\beta_1 k_1/k_e)^2 + (\beta_3 k_3/k_e)^2]^{7/3}}, \tag{15}$$

where the subscript "aniso" denotes an anisotropic expression of a quantity. Λ_2 becomes dependent on β_1 and β_2, i.e.

$$\Lambda_{2\text{aniso}} = \frac{55\ \Gamma(1/3)}{108\sqrt{\pi}\ \Gamma(17/6)}\frac{1}{k_e}\beta_2 \frac{3+11(\beta_1 k_c/k_e)^2}{3+8(\beta_1 k_c/k_e)^2}\frac{1}{\sqrt{1+(\beta_1 k_c/k_e)^2}}, \tag{16}$$

where $k_c = \omega/U_c$ is the convective wavenumber. Equations 6 and 9 are used by the FB-Aniso model to estimate k_e and $\langle u_2^2\rangle$ respectively.

The anisotropic corrections suggested by Kamruzzaman et al. [19] is based on the derivation of a semi-empirical anisotropy correction factor f_2. This factor is a function of the Reynolds number based on Taylor's microscale Re_λ, which can be found by

$$\begin{aligned}
\lambda_f &= \sqrt{15\,\nu\,\frac{2}{3}\,\frac{k_T}{\epsilon_{\text{mod}}}};\\
\lambda_g &= \lambda_f/\sqrt{2};\\
\sigma &= \sqrt{\frac{2}{3}k_T};\\
Re_\lambda &= \sigma\lambda_g/\nu;\\
f_2 &= {Re_\lambda}^{-0.09}.
\end{aligned} \tag{17}$$

Note the modified ϵ of equation 10 is used. The anisotropic $\langle u_2^2\rangle$ is then estimated as

$$\langle u_2^2\rangle_{\text{aniso}} = \frac{2}{3}k_T f_2. \tag{18}$$

Through this anisotropic $\langle u_2^2\rangle$ and equation 8, an anisotropic form of Λ_2 is derived, i.e.

$$\Lambda_{2\text{aniso}} \approx 0.40\frac{[k_T f_2]^{3/2}}{\epsilon_{\text{mod}}} \approx 0.75\frac{[\langle u_2^2\rangle_{\text{aniso}}]^{3/2}}{\epsilon_{\text{mod}}}. \tag{19}$$

Comparing equation 19 to equation 8, the anisotropy correction factor for a length scale is therefore given by $f_L = [f_2]^{3/2}$. Based on this, an anisotropic form of Φ_{22} is derived, such that

$$\Phi_{22\text{aniso}} = \frac{4}{9\pi}\left(\frac{1}{k_e}\right)^2 {f_L}^2 \frac{(f_L k_1/k_e)^2 + (f_L k_3/k_e)^2}{[1+(f_L k_1/k_e)^2 + (f_L k_3/k_e)^2]^{7/3}}, \tag{20}$$

which is identical to equation 15 of the FB-Aniso model for $f_L = \beta_1 = \beta_3$.

2.3. The Current Modified TNO Model

The current modified TNO model is developed from Bertagnolio anisotropic TNO model [20] due to its good delta noise prediction ability (see section 4.1). The first modification is applied to the vertical Reynolds stress component $\langle u_2^2\rangle$. In

FB-Aniso, the isotropic formulation of $\langle u_2^2 \rangle$ (equation 9) is retained. In the current modified TNO model, the approximate ratio of the normal Reynolds stress components for an anisotropic flow over a flat plate [21] is used, such that

$$\langle u_1^2 \rangle : \langle u_2^2 \rangle : \langle u_3^2 \rangle = 4 : 2 : 3. \tag{21}$$

Hence the anisotropic $\langle u_2^2 \rangle$ is given by

$$\langle u_2^2 \rangle_{\text{aniso}} = \frac{4}{9} k_T. \tag{22}$$

Note that these anisotropic normal Reynolds stresses ratios are not constant across the thickness of a real BL, they are also not universal for all BL flows and are strongly influenced by mean pressure gradient, compressibility as well as flow and surface conditions further upstream in the BL. However, the use of simple approximations such as equation 21 is more suitable for industrial wind turbine engineering applications compared to using advanced numerical simulations which are too time-consuming.

The second modification is the introduction of new stretching factors in the streamwise, vertical and spanwise directions. An anisotropic formulation for k_e can be derived by applying the current anisotropic $\langle u_2^2 \rangle$ to equations 7 and 19, such that

$$k_{e,\text{aniso}} = \frac{\sqrt{\pi}\ \Gamma(5/6)}{\Gamma(1/3)} \left[0.75\ \frac{[(4/9)k_T]^{3/2}}{\epsilon} \right]^{-1}.$$

Note that unlike MK-Iso and MK-Aniso, the computed mean energy dissipation rate ϵ is used directly without any modification. A similar equation can be derived for the isotropic k_e by using the isotropic formulation of $\langle u_2^2 \rangle$ (equation 9), such that

$$k_e = \frac{\sqrt{\pi}\ \Gamma(5/6)}{\Gamma(1/3)} \left[0.75\ \frac{[(2/3)k_T]^{3/2}}{\epsilon} \right]^{-1}.$$

Therefore, $k_{e,\text{aniso}}$ is related to the isotropic k_e by

$$k_{e,\text{aniso}} = \left(\frac{3}{2} \right)^{3/2} k_e\,. \tag{23}$$

The anisotropy correction of FB-Aniso is based on stretching factors that are used to scale the isotropic k_e in equations 15 and 16 for Φ_{22} and Λ_2 respectively. The current model also employs these two equations for the computations of Φ_{22} and Λ_2. However, k_e is further scaled by a factor of $(3/2)^{3/2}$ as shown by equation 23 in the current model. Hence, three new stretching factors are derived based on equations 11 to 13, such that

$$\beta_{1,\text{new}} = \left(\frac{3}{2} \right)^{-3/2} \Theta\,; \tag{24}$$

$$\beta_{2,\text{new}} = \left(\frac{3}{2} \right)^{-3/2} \gamma^{1/5}\,; \tag{25}$$

$$\beta_{3,\text{new}} = \left(\frac{3}{2} \right)^{-3/2} (2\gamma)^{1/2}\,, \tag{26}$$

where γ is the non-dimensional mean pressure gradient as defined in equation 14, and the parameter Θ is different to the value of $\beta_1 = 0.4$ used in FB-Aniso, which was set by comparing the computed and the measured one-point k_1 wavenumber auto-spectra of u_2 at several wind speeds and angles of attack for a NACA0015 aerofoil [20]. The current value of Θ cannot be disclosed due to confidentiality agreement. It will be shown in section 4 that the current modifications lead to very good agreements between the predicted and measured SPL spectra for many test cases, which include ten different aerofoils under various flow configurations.

3. COMPARISONS OF THE CURRENT AERODYNAMIC PREDICTIONS TO MEASUREMENTS

The BL aerodynamic prediction module of the current code is based on the BL prediction codes EDDYBL [21] and XFoil [22]. For all the aerodynamic calculations in the current paper, the EDDYBL Wilcox k-ω turbulence model is employed. To estimate the BL properties near the TE, a preliminary XFoil calculation is carried out to provide the initial and boundary conditions required by the EDDYBL part of the code. For clean BL conditions, EDDYBL is used to calculate the BL flow from a short distance aft of the BL transition location estimated by XFoil to the TE. For tripped BL conditions, BL tripping on both sides of an aerofoil is enforced in the same way as a normal XFoil calculation, then EDDYBL is used to calculate the BL flow from a short distance aft of the BL trip location to the TE on each side of the aerofoil.

To show the validity of the current aerodynamic calculation method, the profiles of U_1/U_∞, $\langle u_2^2 \rangle$, k_T and ϵ across the BL near the TE on the aerofoil suction side for the test cases shown in table I are computed and compared with experimental measurements. For ϵ, the predicted profiles directly from the current code and the modified ϵ suggested by Kamruzzaman et al. [19] (equation 10) are compared to the experimental measurements. For $\langle u_2^2 \rangle$, the anisotropic formulations of the current modified and the MK-Aniso TNO models by equation 22 and 18 respectively are compared to the measurements. The experimental measurements for the NACA64$_3$-418 aerofoil are obtained from Ref [19], and the NACA0012 aerofoil cases with $\alpha = 0^\circ$ and 4° are the BANC-II workshop [25] cases 1 and 2 respectively. These experimental measurements were obtained using the Laminar Wind Tunnel (LWT) at the University of Stuttgart.

Aerofoil	c [m]	L [m]	U_∞ [m/s]	Effective α [$^\circ$]	Suction-side Trip x/c	Pressure-side Trip x/c	r_o [m]	Tunnel
NACA64$_3$-418	0.6	1.0	62.0	0.0	n/a	n/a	1.00	LWT
NACA64$_3$-418	0.6	1.0	62.0	0.0, 3.0	0.05	0.05	1.00	LWT
NACA0012	0.4	1.0	56.0	0.0	0.065	0.065	1.00	LWT
NACA0012	0.4	1.0	54.8	4.0	0.065	0.065	1.00	LWT

Table I. Test cases for the comparisons between the predicted and the measured BL flow properties near the TE

Figures 2 to 5 show the comparisons for the NACA64$_3$-418 aerofoil, and those for the NACA0012 aerofoil are shown in figures 6 to 9. From figures 2 and 6, it can be seen that the current predictions of U_1/U_∞ show good agreement with the experimental measurements. Also, the BL thickness predicted by the current code is similar to the measurements in general. The measured U_1 at the edge of the BL are higher for all cases. This could be caused by the extra flow acceleration due to the presence of the wind tunnel wall. Figures 3 and 7 show that the current anisotropic $\langle u_2^2 \rangle$ formulation produces very similar estimations to the anisotropic corrections used in the MK-Aniso TNO model. It can also be seen that the current predicted $\langle u_2^2 \rangle$ profiles have lower level around the peak compared to the measurements, particularly for the cases with non-zero α. Although the peak levels for some cases are different, both predictions and measurements show an increase in peak level for higher α. Similar level of agreement and trend due to increasing α can be observed for k_T from figures 4 and 8. For ϵ, it can be seen from figures 5 and 9 that the current directly-calculated profiles show reasonable agreement with measurements. The modification suggested by Kamruzzaman et al. [19] does lead to closer agreement with measurements close to the wall, but this modification leads to much lower level of ϵ for other part across the BL thickness for some cases. These comparisons also show that the current XFoil pre-calculation is suitable for both tripped and clean BL conditions.

The BL properties extraction x/c location for TE noise computation is at 0.995 if possible. However, the flow near the TE might be separated at high angle of attack. If the flow separation is too severe, the current aerodynamic code could fail and the run would terminate before the end. When the separation is not too extensive, the code can still return estimated BL properties, but the extraction x/c location could be moved upstream of 0.995. For the aerodynamic calculations in this section, the furthest upstream extraction x/c is 0.989 for the NACA64$_3$-418 aerofoil with clean BL at $\alpha = 0^\circ$. The effects of separated flow of various extent on noise prediction will be shown and discussed in greater details in section 4.2.

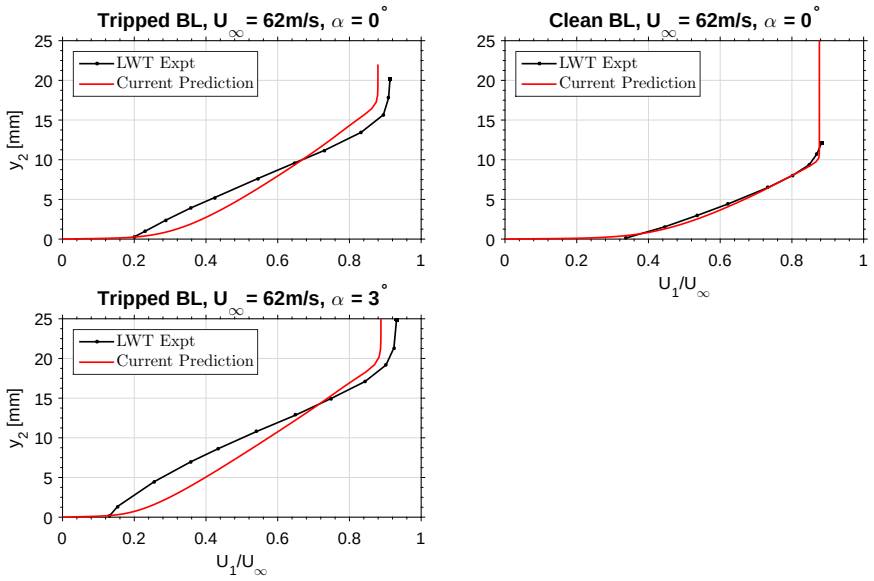

Figure 2. Comparisons of the predicted and measured U_1/U_∞ profiles for the NACA64$_3$-418 aerofoil

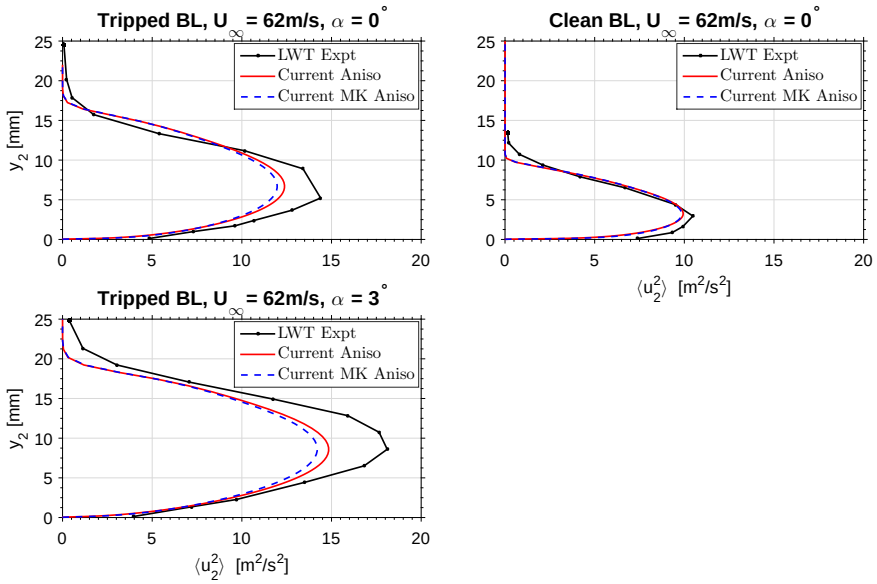

Figure 3. Comparisons of the predicted and measured $\langle u_2^2 \rangle$ profiles for the NACA64$_3$-418 aerofoil

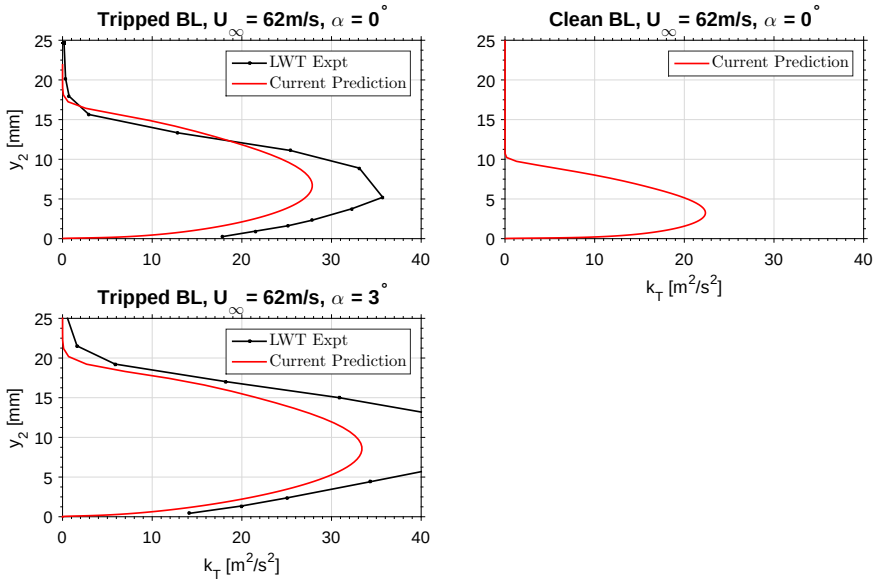

Figure 4. Comparisons of the predicted and measured k_T profiles for the NACA64$_3$-418 aerofoil

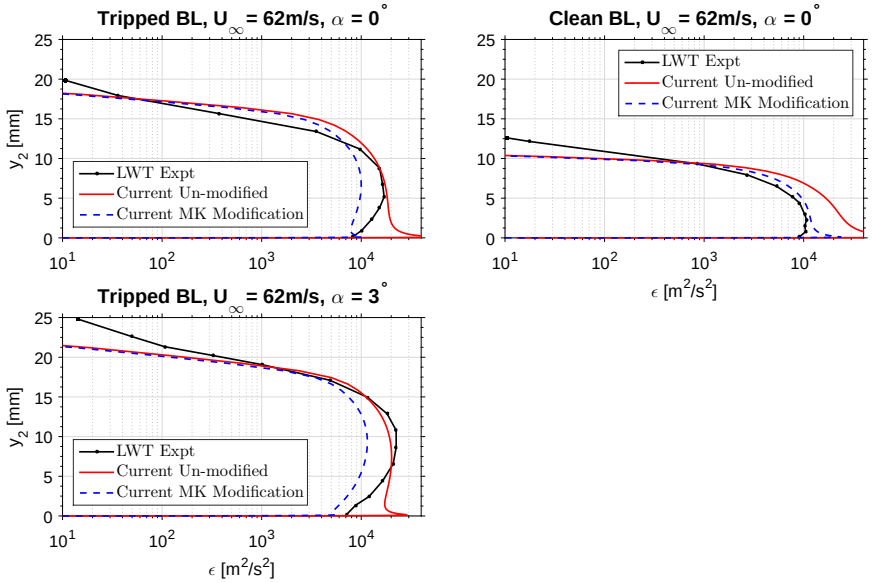

Figure 5. Comparisons of the predicted and measured ϵ profiles for the NACA64$_3$-418 aerofoil

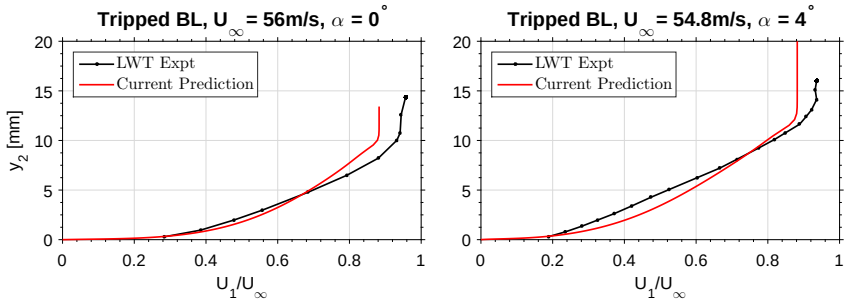

Figure 6. Comparisons of the predicted and measured U_1/U_∞ profiles for the NACA0012 aerofoil

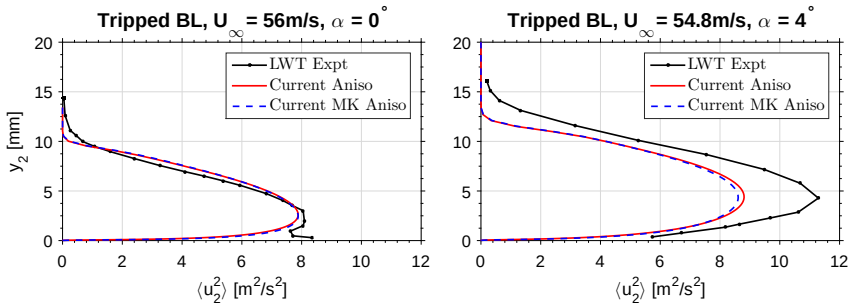

Figure 7. Comparisons of the predicted and measured $\langle u_2^2 \rangle$ profiles for the NACA0012 aerofoil

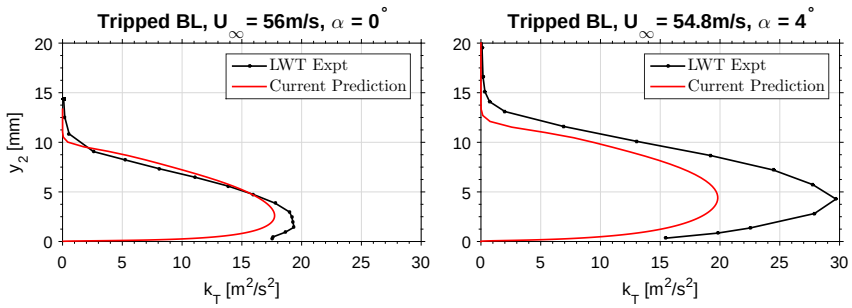

Figure 8. Comparisons of the predicted and measured k_T profiles for the NACA0012 aerofoil

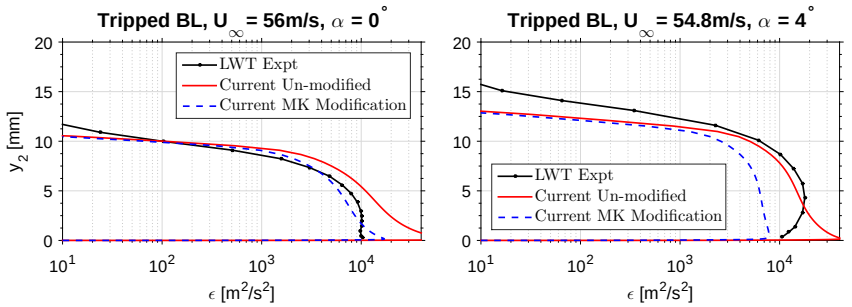

Figure 9. Comparisons of the predicted and measured ϵ profiles for the NACA0012 aerofoil

4. THE TRAILING-EDGE NOISE PREDICTION CAPABILITIES OF THE FIVE TNO MODEL VARIANTS

For the current analyses, the experimental measurements from two wind tunnels are used: the open-return Laminar Wind Tunnel (LWT) with a closed test section at the University of Stuttgart and the closed-return Stability Wind Tunnel (SWT) at Virginia Tech.

For the LWT experiments, the coherent particle velocity (CPV) method [26, 27] was used to measure the TE noise. This measurement method is based on a cross-spectral analysis of two hot-wire sensor signals placed on the suction- and the pressure-sides of the aerofoil TE. The low frequency ($<$ 1000Hz) measurements by the CPV method are known to be disturbed by hydrodynamic fluctuations [27], hence they can only be used as rough indications of the spectral trend. The diffuser section of the LWT has been lined with acoustic-absorbing material to reduce noise originating from the fan. For the tripped condition, STREIFENEDER ZigZag tape with an opening angle of 60°, a thickness of 0.38mm and a streamwise extent of 11mm were used. The BL trip location is taken as the leading-edge of the tape.

For the SWT, a microphone array located in an anechoic chamber to a side of the acoustically-treated test section is used for TE noise measurements [28, 29]. For the tripped condition, serrated trip tape (Glasfaser-Flugzeug-Service GmbH 3D Turbulator Tape) with a thickness of 0.5mm and an overall width of 12mm were used. The leading- and trailing-edges are cut to form aligned serrated edges with a 6mm distance between points. The BL trip location is taken as the leading-edge of the tape.

4.1. SPL Difference between Two Different Aerofoils with Similar Lift Coefficients

In wind turbine blade design, the blade cross-sections change until an optimised design is obtained. When minimising TE noise is a target criterion, it is crucial that a model is able to predict accurately whether the TE noise level is increased or decreased due to a change in the cross-sectional geometry at some spanwise location. Hence the ability of a model to predict accurately the difference in SPL between two aerofoils at similar lift coefficients within a certain frequency range is important.

For this delta noise analysis, seven aerofoils grouped into 35 pairs (two aerofoils with similar lift coefficients are grouped as a pair) are analysed. Of these 35 pairs, 26 and 9 are from the LWT and the SWT tests respectively. 15 of the 26 LWT pairs are for clean BL condition, and the remaining 11 are for tripped BL condition. All nine SWT pairs are for clean BL condition.

The current study defines two parameters to aid determining delta noise prediction accuracy. The first one is Δ_{OASPL}, which is an overall SPL difference based on the A-weighted spectra, i.e.

$$\Delta_{\text{OASPL}} = 10\log_{10}\left[\sum_{i=1}^{n} 10^{(\text{SPL}_{2,i}/10)}\right] - 10\log_{10}\left[\sum_{i=1}^{n} 10^{(\text{SPL}_{1,i}/10)}\right] \ , \tag{27}$$

where n is the number of discrete frequency bands, and $\text{SPL}_{1,i}$ and $\text{SPL}_{2,i}$ are the A-weighted SPL of aerofoil one and two respectively at the i^{th} frequency band. Note that the contribution of each frequency band is added by first converting the SPL to mean square pressure.

The second one is Δ_{dBsum}, which is the difference between the sums of the A-weighted SPL in dB(A) of the two aerofoils, i.e.

$$\Delta_{\text{dBsum}} = \sum_{i=1}^{n} \text{SPL}_{2,i} - \sum_{i=1}^{n} \text{SPL}_{1,i} \ . \tag{28}$$

The same frequency ranges are used for both Δ_{OASPL} and Δ_{dBsum} calculations. For the LWT cases, the frequency range considered is between 1000 and 3150Hz since the measurements below 1000Hz is not as accurate. For the SWT cases, frequencies between 630 and 3150Hz are considered.

The general SPL spectral shape for aerofoil TE noise can be seen from the spectra in figure 1 in section 2 and later in section 4.2. Since spectral peaks usually occur below 1000Hz, the lower frequency bands have much greater effects on the sign of Δ_{OASPL} than the higher frequency bands. This is demonstrated in figure 10, which shows two hypothetical SPL spectra and the corresponding Δ_{OASPL} and Δ_{dBsum} values. It can be seen that Spectrum 2 has lower SPL than Spectrum 1 at all frequency bands except for at 1000Hz. However, due to the shape of this kind of spectra, the sign of Δ_{OASPL} for Spectrum 2 relative to Spectrum 1 is positive since the overall SPL for Spectrum 2 is higher. On the other hand, the sign of Δ_{dBsum} for Spectrum 2 relative to Spectrum 1 is negative, which is a better reflection of the relative magnitude of the two spectra over the frequency range considered. Therefore, Δ_{dBsum} is also used in the current study to investigate the delta noise prediction ability of the five models.

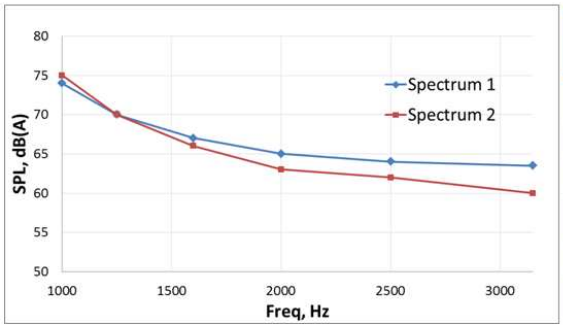

Freq, Hz	Spectrum 1, dB(A)	Spectrum 2, dB(A)
1000	74.0	75.0
1250	70.0	70.0
1600	67.0	66.0
2000	65.0	63.0
2500	64.0	62.0
3150	63.5	60.0

Spectrum 2 relative to Spectrum 1

Δ_{OASPL}, dB(A)	Δ_{dBsum}, dB(A)
0.19	-7.5

Figure 10. The Δ_{OASPL} and Δ_{dBsum} values for two hypothetical SPL spectra

A prediction is deemed correct when the sign of a delta noise parameter is the same as the corresponding parameter derived from the measured data. Figure 11 shows the number of correct Δ_{OASPL} and Δ_{dBsum} sign predictions by the five models. The lefter-most bar in each of the two bar charts is the reference total of 35. The compositions of the correct sign predictions with regards to wind tunnel used and BL condition are also presented. It can be seen that the current modified, FB-Aniso and FB-Iso models have the highest Δ_{OASPL} and Δ_{dBsum} sign prediction accuracies. For Δ_{OASPL}, these three models predict the correct sign for 22 out of 35 aerofoil pairs. For Δ_{dBsum}, 25 out of 35 pairs are correctly predicted. Hence, the Δ_{OASPL} and Δ_{dBsum} sign prediction accuracies of these three models are 62.9% and 71.4% respectively. MK-Iso has the second lowest Δ_{OASPL} and Δ_{dBsum} sign prediction accuracies of 54.3% and 62.9% respectively. MK-Aniso has the lowest sign prediction accuracies of 40.0% and 51.4% for Δ_{OASPL} and Δ_{dBsum} respectively.

In general, the sign prediction accuracies for Δ_{OASPL} by the five models are lower than those for Δ_{dBsum}. It is found that this is mainly due to the LWT aerofoil pairs with clean BL condition at $\alpha > 8^\circ$. The better Δ_{dBsum} sign prediction accuracies for these cases suggest two possible situations. The first one is that for the higher frequency bands, the predicted and measured dB(A) sum differences between many aerofoils are rooted deeply on the same side, i.e. either very negative or very positive, so that the discrepancy in the vicinity of 1000Hz cannot undermine the overall sign agreement. The second one is that the better Δ_{dBsum} sign agreement is due to luck. Figure 12 shows the normalised SPL spectra of one of the aerofoil pairs of these LWT cases between 1000 and 3150Hz. $\alpha = 8.9^\circ$ and 8° for the RisoB1-18 and A-18 aerofoils respectively. Both aerofoils have the same thickness to chord ratio of 18%. The freestream velocity U_∞ is 70m/s. The maximum experimentally-measured SPL value for the RisoB1-18 aerofoil is used to normalised all the spectra in the figure. The measured Δ_{dBsum} of the A-18 aerofoil relative to the RisoB1-18 aerofoil is positive, and the corresponding measured Δ_{OASPL} is negative. All five models predict the correct sign for Δ_{dBsum} only. It can be seen that for this aerofoil pair, the predictions of the current modified and FB-Aniso models fit the first situation due to their very good predictions

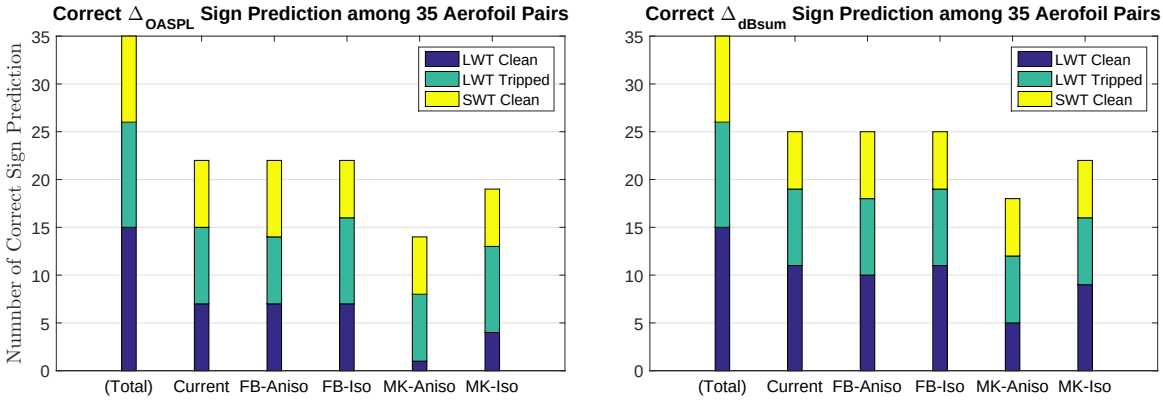

Figure 11. The correct Δ_{OASPL} and Δ_{dBsum} sign prediction for the five TNO model variants tested

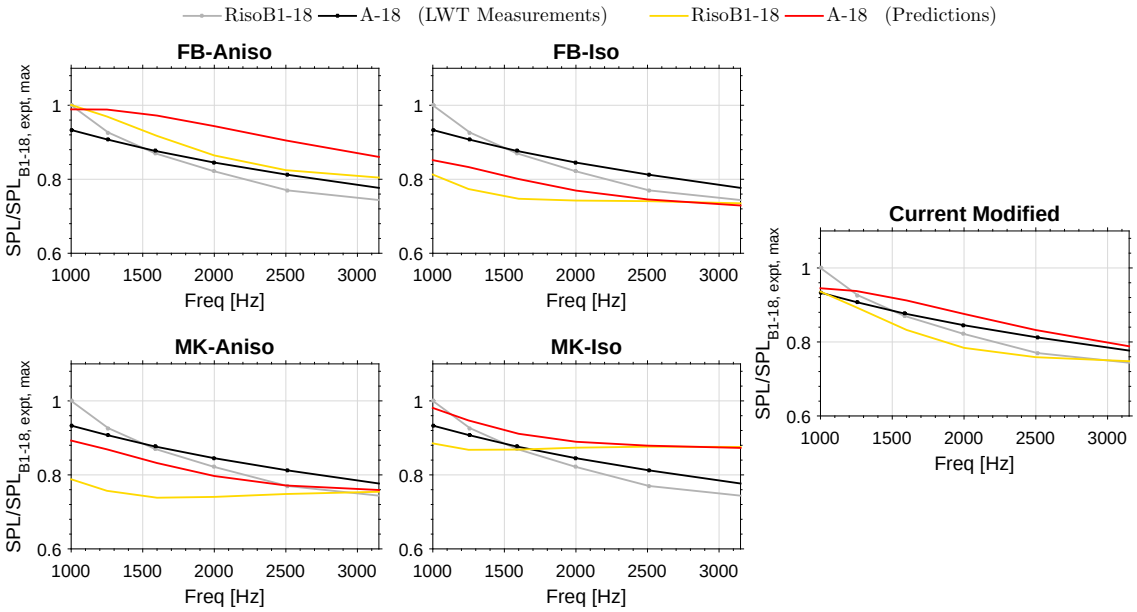

Figure 12. The LWT-measured and model-predicted normalised SPL spectra for an aerofoil pair with clean BL condition at $\alpha > 8°$

of the relative SPL at the higher frequency bands, and the second situation fits the predicted spectra by FB-Iso, MK-Iso and MK-Aniso models, which show nearly the opposite trend in relative SPL between the two aerofoils.

The different sign prediction accuracies between FB-Iso and MK-Iso suggest that the use of the modified ϵ by equation 10 in MK-Iso reduces delta noise prediction accuracy. The lowest delta noise prediction accuracy of MK-Aniso is related to the anisotropy correction applied in that model. Although FB-Aniso and FB-Iso models have good delta noise prediction ability, it will be shown in the next sub-section that their predicted SPL spectra usually show larger discrepency to the experimental measurements compared to the current modified model.

4.2. Closeness of the Predicted and Measured Far-Field SPL Spectra

The closeness of the predicted far-field SPL spectra to the measurements is important when the integrated noise level over some frequency range of a wind turbine aerofoil, blade or rotor is required. The 65 test cases analysed are listed in Table II, where 'SS Trip x/c' and 'PS Trip x/c' denote the x/c locations of BL trip on the suction-side and the pressure-side respectively, and 'Group' refers to the 18 case groups that the test cases are organised into. LWT measurements are used

for case groups 1.1 to 7.2, which contains 40 test cases. The remaining 25 test cases in case groups 8.1 to 10.1 employ SWT measurements. Seven aerofoils are employed in the analysis. The A-18 and A-21 aerofoils have thickness to chord ratios of 18% and 21% respectively, and are used in modern large wind turbines. The data for case groups 1.1 and 1.2 are from Ref. [19], while those for case groups 2.1, 2.2 and 3.1 are from the BANC-II workshop [25] cases 1, 2 and 5 respectively. For case groups 4.1 to 10.1, the data were measured by Vestas in the LWT and SWT.

For each case group, the maximum measured SPL value among all its test cases is used to normalise the measured and the predicted SPL spectra. Figures 13 to 29 show the measured and the predicted spectra by the five TNO model variants tested. It can be seen from these figures that the predicted SPL spectra by the current modified TNO model show the best agreement with the experimental measurements in terms of both spectral shape and magnitude for most of the test cases analysed.

Group	Aerofoil	c [m]	U_∞ [m/s]	Effective α [°]	SS Trip x/c	PS Trip x/c	r_o [m]	Tunnel	Fig.
1.1	NACA64$_3$-418	0.6	70.0	0.0	n/a	n/a	1.00	LWT	13
1.2	NACA64$_3$-418	0.6	70.0	0.0, 3.0	0.05	0.05	1.00	LWT	14
2.1	NACA0012	0.4	56.0	0.0	0.065	0.065	1.00	LWT	15
2.2	NACA0012	0.4	54.8	4.0	0.065	0.065	1.00	LWT	15
3.1	DU-96-180	0.3	60.0	4.0	0.12	0.15	1.00	LWT	16
4.1	RisoB1-15	0.6	70.0	3.0, 6.0, 9.0, 12.0	n/a	n/a	1.00	LWT	17
4.2	RisoB1-15	0.6	70.0	3.0, 6.0, 9.0, 11.0	0.05	0.10	1.00	LWT	18
5.1	RisoB1-18	0.6	70.0	3.4, 5.1, 7.1, 8.9	n/a	n/a	1.00	LWT	19
5.2	RisoB1-18	0.6	70.0	3.4, 5.1, 7.1, 8.9	0.05	0.10	1.00	LWT	20
6.1	A-18	0.6	70.0	2.0, 4.0, 6.0, 8.0, 9.0	n/a	n/a	1.00	LWT	21
6.2	A-18	0.6	70.0	2.0, 4.0, 6.0, 8.0, 9.0	0.05	0.10	1.00	LWT	22
7.1	A-21	0.6	70.0	2.7, 4.6, 6.5, 8.9	n/a	n/a	1.00	LWT	23
7.2	A-21	0.6	70.0	2.7, 4.6, 6.5, 8.9	0.05	0.10	1.00	LWT	24
8.1	RisoB1-18	0.918	28.0	-0.69, 3.79, 6.61, 10.53, 13.58	n/a	n/a	1.83	SWT	25
8.2	RisoB1-18	0.918	28.0	-0.69, 3.79, 6.61, 10.53, 13.58	0.05	0.10	1.83	SWT	26
9.1	RisoB1-18	0.918	56.0	-0.26, 3.23, 5.95, 8.78, 12.82	n/a	n/a	1.83	SWT	27
9.2	RisoB1-18	0.918	56.0	-0.26, 3.23, 5.95, 8.78, 12.82	0.05	0.10	1.83	SWT	28
10.1	A-18	0.914	51.6	-1.6, 1.1, 2.9, 4.6, 5.6	n/a	n/a	1.90	SWT	29

Table II. Test cases for the closeness of the predicted and measured far-field SPL spectra

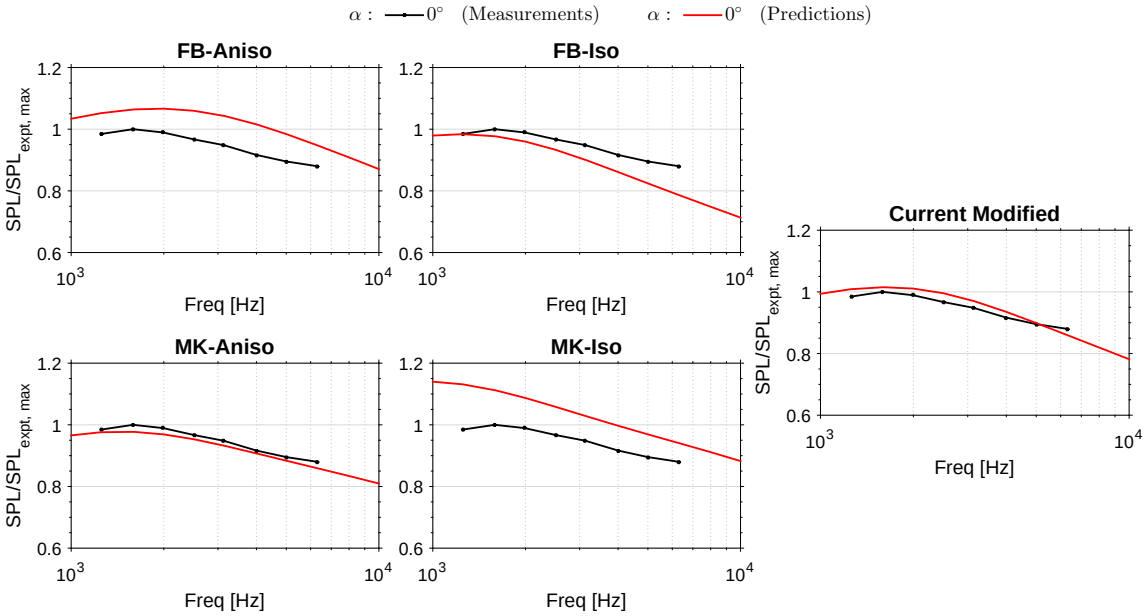

Figure 13. Case group 1.1 for a NACA64$_3$-418 aerofoil with $U_\infty = 70$m/s and clean BL (1/3 octave)

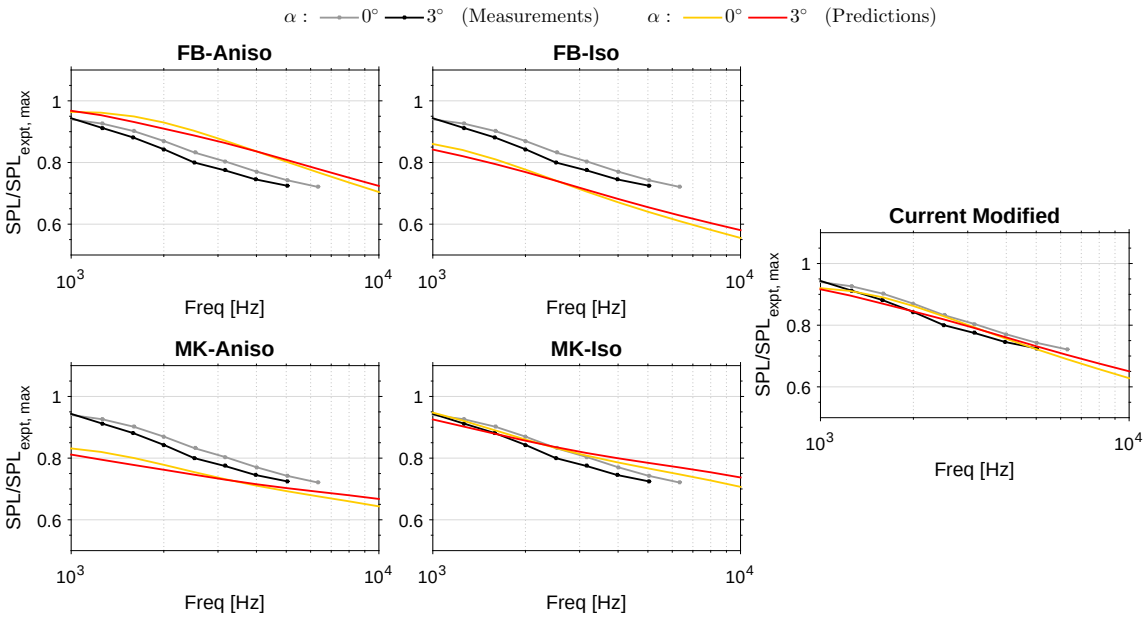

Figure 14. Case group 1.2 for a NACA64$_3$-418 aerofoil with $U_\infty = 70$m/s and tripped BL (1/3 octave)

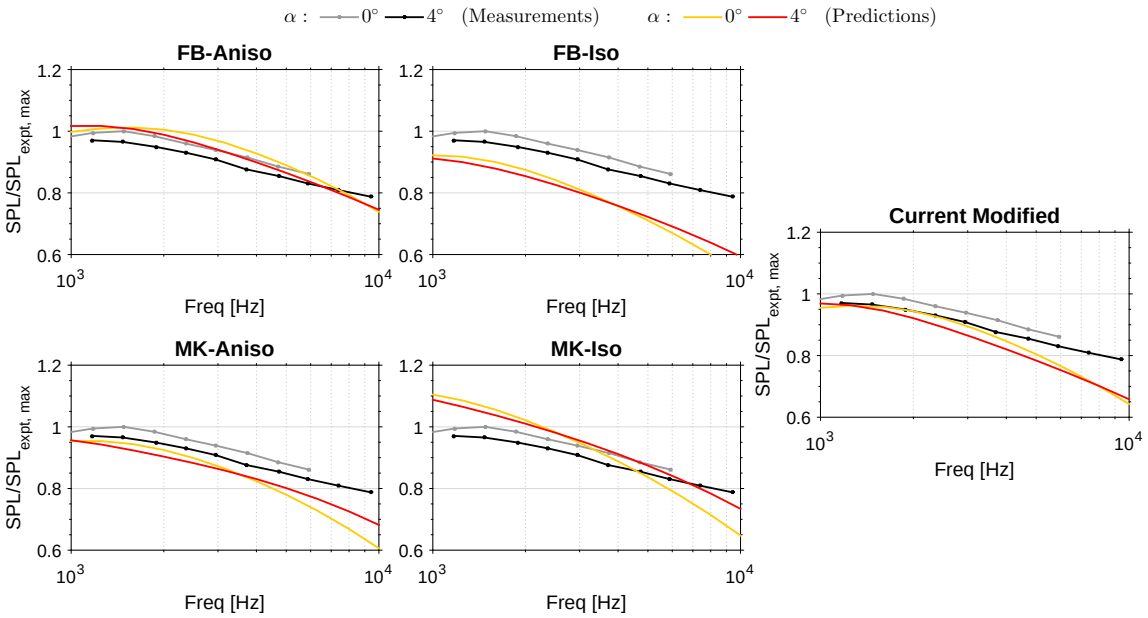

Figure 15. Case groups 2.1 and 2.2, with $U_\infty = 56$m/s and 54.8m/s respectively, for a NACA0012 aerofoil with tripped BL (1/3 octave)

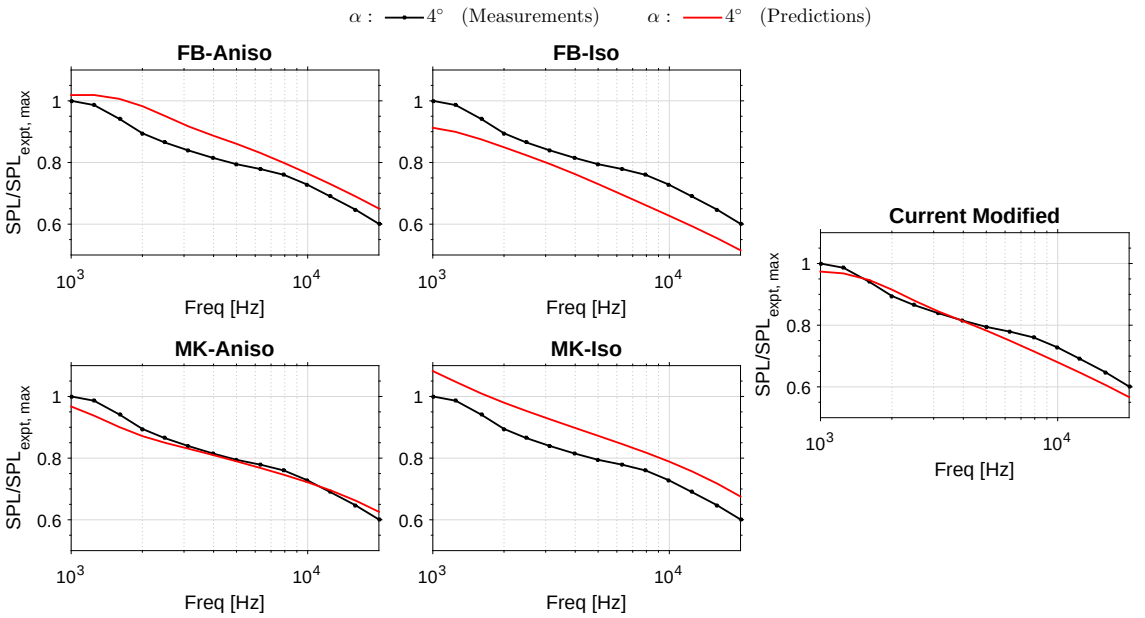

Figure 16. Case group 3.1 for a DU-96-180 aerofoil with $U_\infty = 60$m/s and tripped BL (1/3 octave)

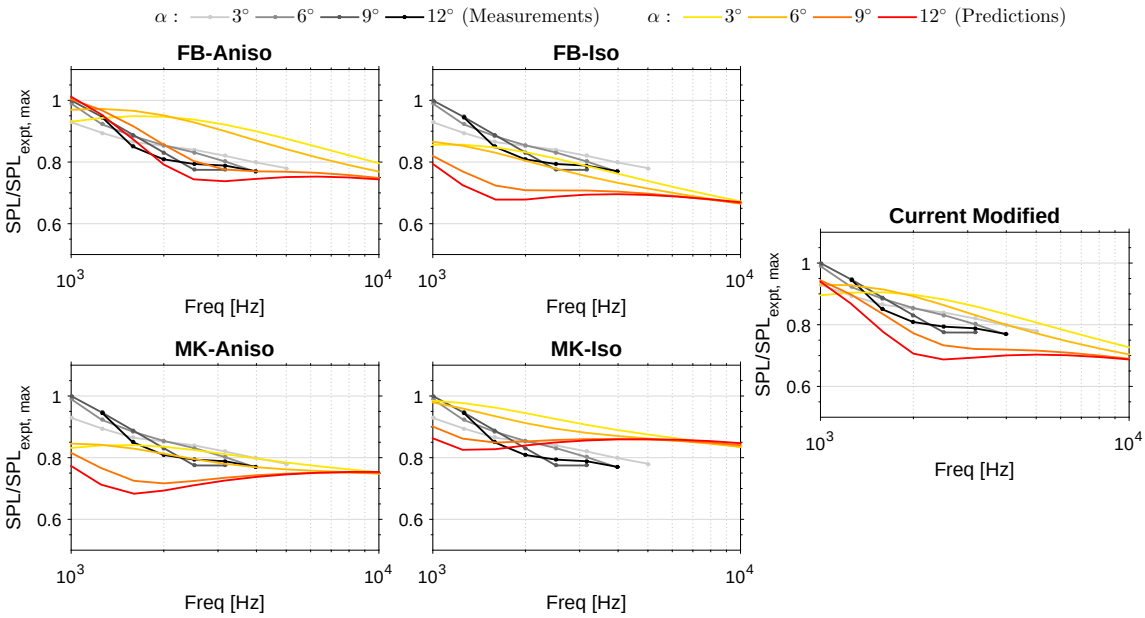

Figure 17. Case group 4.1 for a RisoB1-15 aerofoil with $U_\infty = 70$m/s and clean BL (1/3 octave)

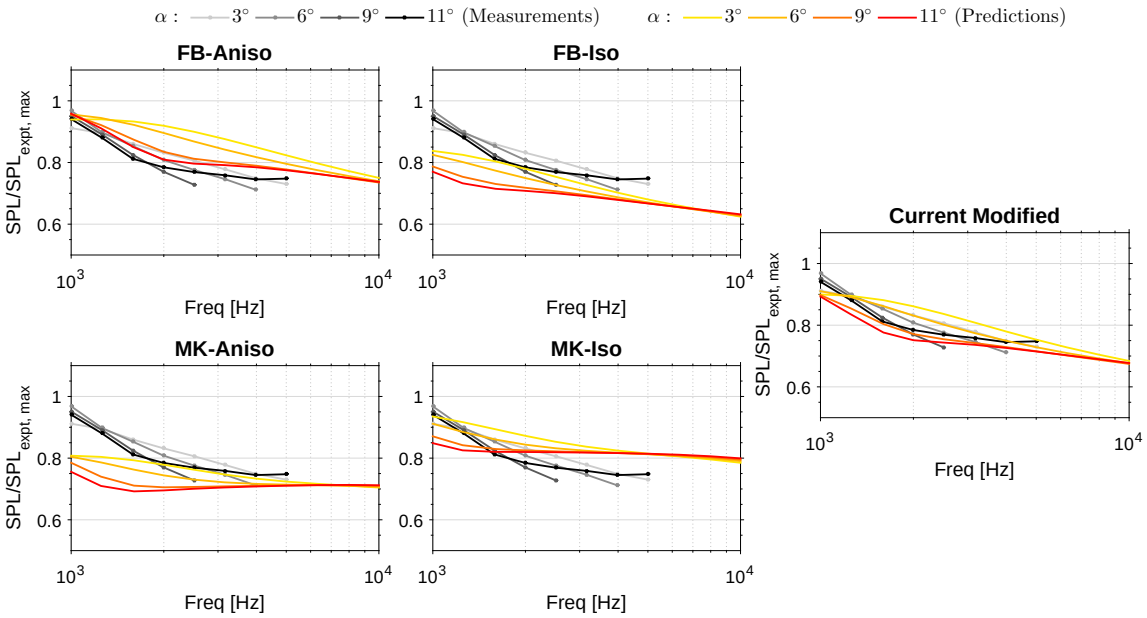

Figure 18. Case group 4.2 for a RisoB1-15 aerofoil with $U_\infty = 70$m/s and tripped BL (1/3 octave)

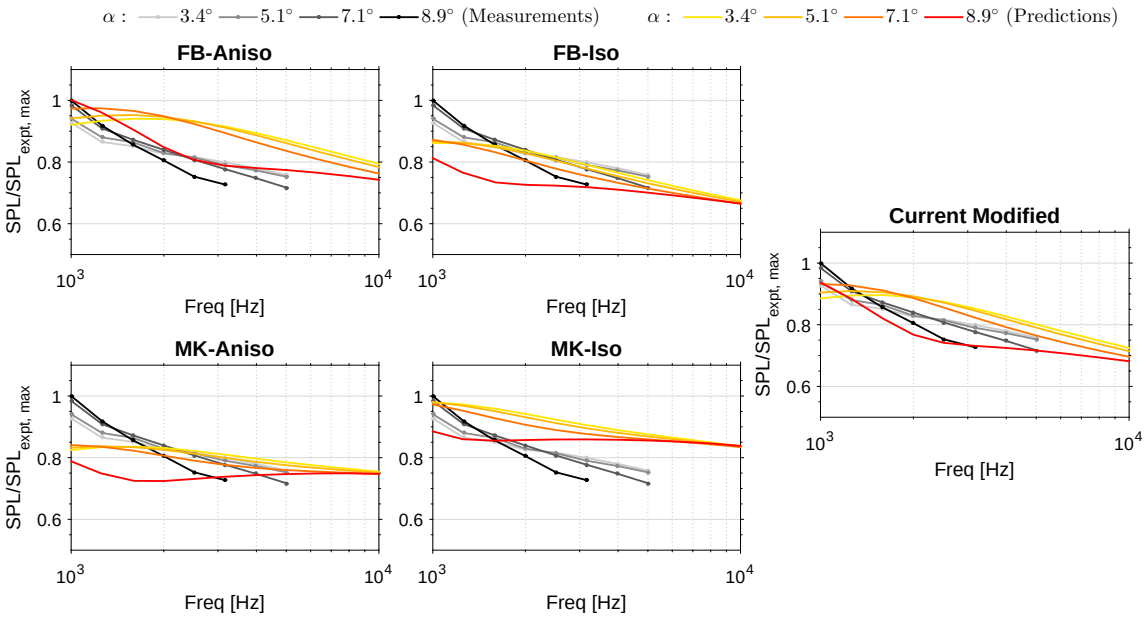

Figure 19. Case group 5.1 for a RisoB1-18 aerofoil with $U_\infty = 70$m/s and clean BL (1/3 octave)

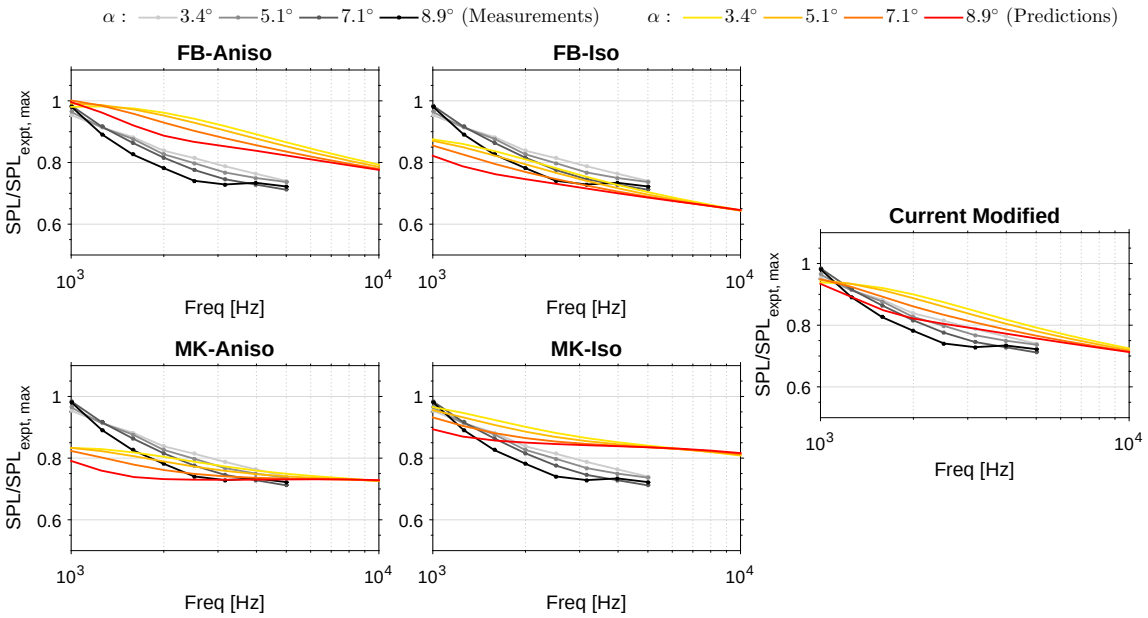

Figure 20. Case group 5.2 for a RisoB1-18 aerofoil with $U_\infty = 70$m/s and tripped BL (1/3 octave)

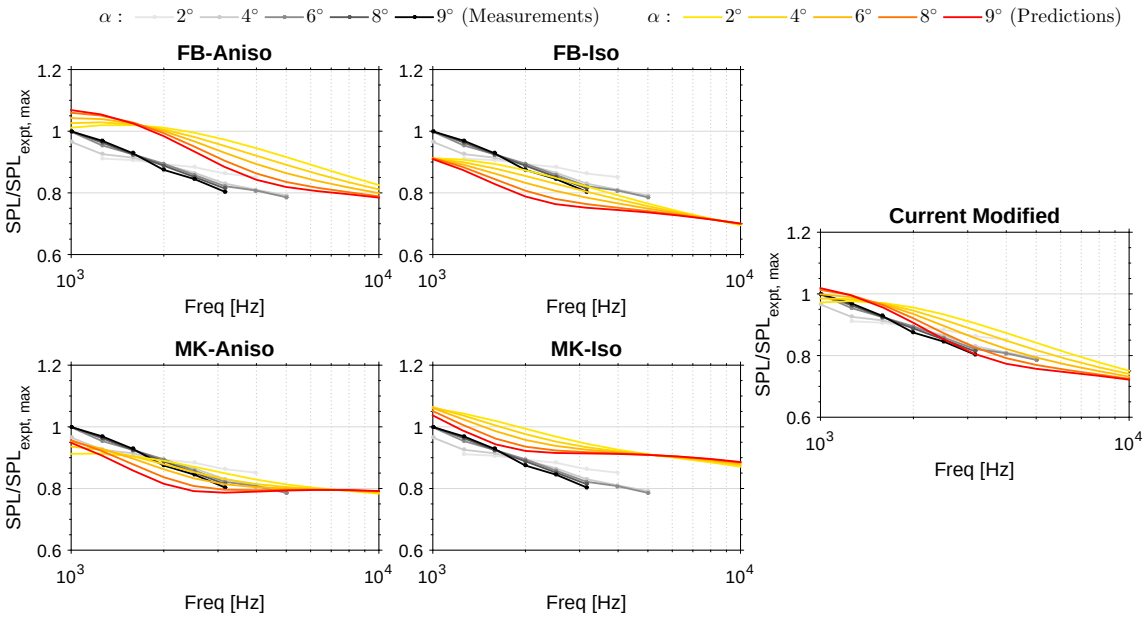

Figure 21. Case group 6.1 for an A-18 aerofoil with $U_\infty = 70$m/s and clean BL (1/3 octave)

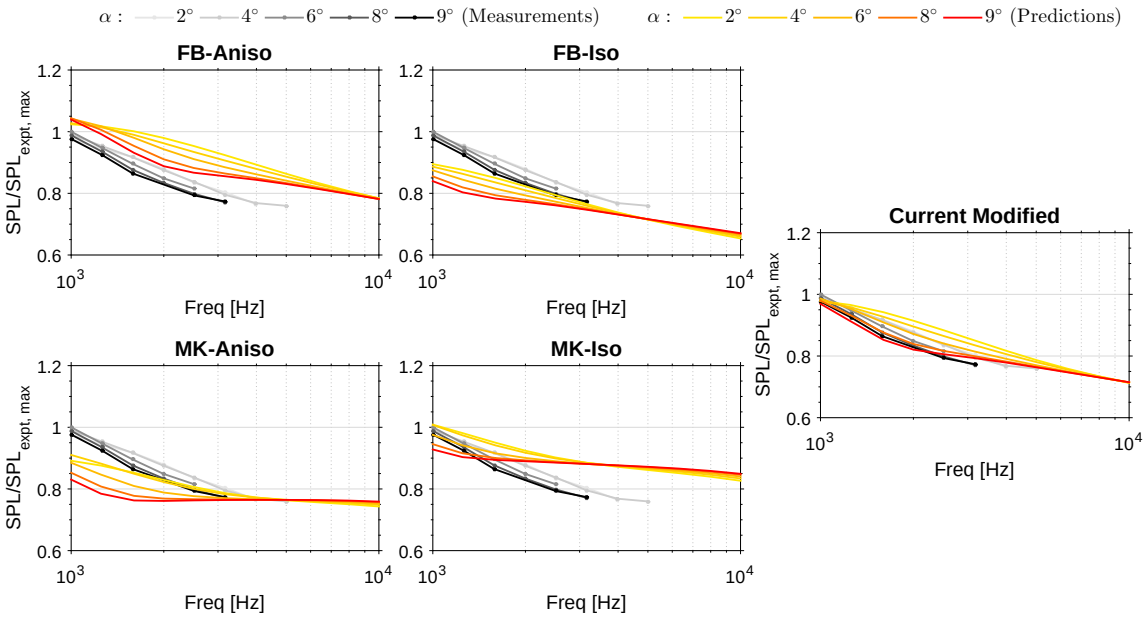

Figure 22. Case group 6.2 for an A-18 aerofoil with $U_\infty = 70$m/s and tripped BL (1/3 octave)

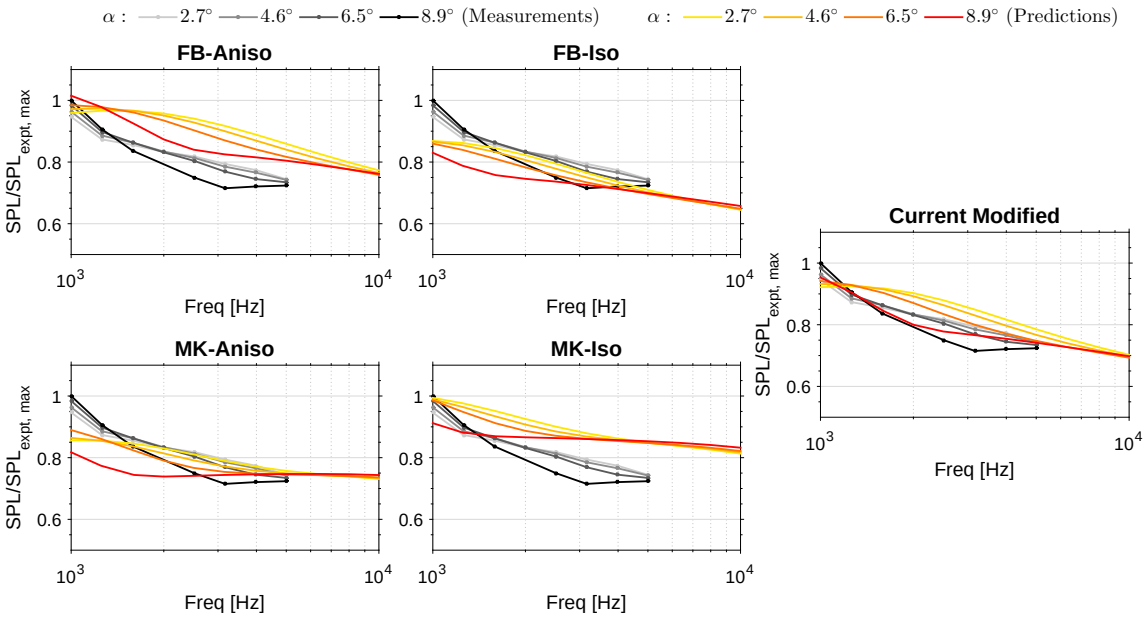

Figure 23. Case group 7.1 for an A-21 aerofoil with $U_\infty = 70$m/s and clean BL (1/3 octave)

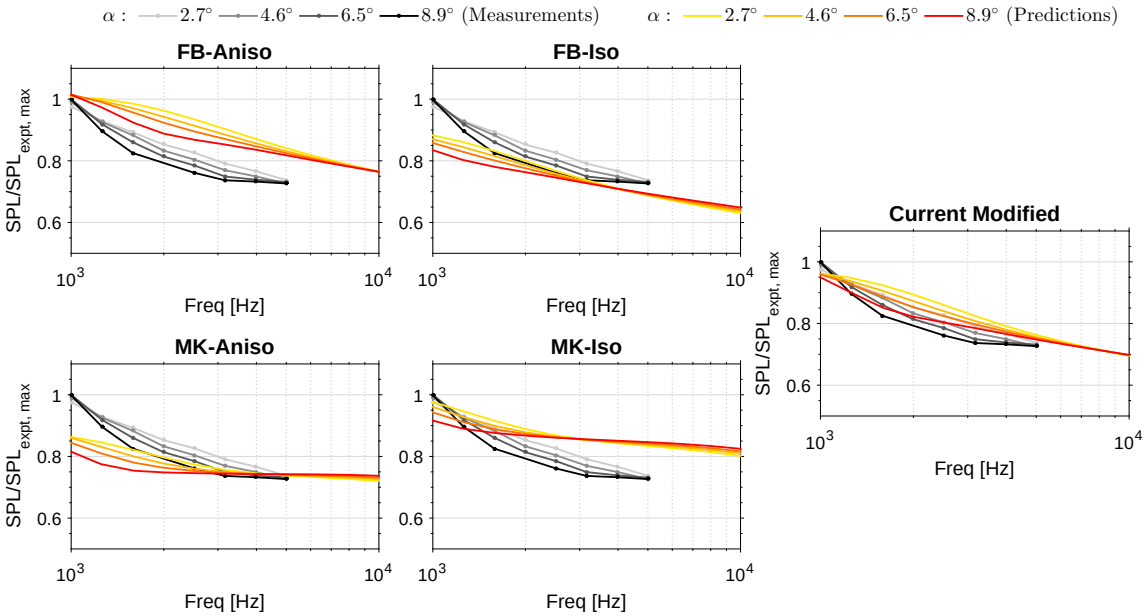

Figure 24. Case group 7.2 for an A-21 aerofoil with $U_\infty = 70$m/s and tripped BL (1/3 octave)

The LWT measurements for case groups 4.1 to 7.2 (Re = 3.16×10^6) show that in general, increasing α leads to relatively higher low-frequency noise and lower high-frequency noise. Some cases seemingly show that the SPL for different α tend to similar levels at higher frequencies ($>$ 4000Hz approximately). However, the trend at these higher frequencies is uncertain due to the incompleteness or the lack of LWT measurements available. For all the LWT cases analysed, the current aerodynamic calculation is able to extract BL properties close to the TE. Most extraction locations are beyond $x/c = 0.98$. The furthest from the TE is at $x/c = 0.93$ for case group 4.1 for a RisoB1-15 aerofoil at an α of 12°. It can be seen from figure 17 that for case group 4.1, the change in SPL as α increases (referred to as α-trend herein) is well-predicted by the current modified model although some discrepancy in spectral magnitude between its predictions and measurements can be observed. The α-trend of all LWT measurements is generally captured by the five model predictions, and there is no measurement which shows disproportionately large increase in noise with the same increment in α. This suggests that the noise emitted is dominated by TE noise for all LWT cases. In terms of the prediction of the frequency beyond which SPL becomes lower when α is increased for an aerofoil, the current modified and FB-Aniso TNO show the best performance.

For the SWT measurements, the change in SPL with increasing α follows different trends. Case groups 8.1 and 8.2 for a RisoB1-18 aerofoil with U_∞ of 28m/s (Re = 1.60×10^6) show the reverse trend to the LWT measurements described, i.e. increasing α leads to relatively lower low-frequency noise and higher high-frequency noise. At the highest α of 13.58°, the measured SPL becomes significantly higher over much of the frequency range. This suggests that for this SWT measurement case, flow separation noise replaces TE noise as the main noise generation mechanism. For these two case groups, relatively larger fluctuations in the measured SPL beyond approximately 3000Hz can be observed. At some frequencies in this range, the measured mean square pressure is so small that the corresponding SPL is even negative. Hence the quality of the SWT 1/12 octave data at these frequencies for case groups 8.1 and 8.2 is not as good as the rest of the measured frequency range. For $\alpha = 13.58°$, the current aerodynamic calculation extracts the BL properties at $x/c = 0.738$ and 0.792 for the clean and tripped conditions respectively due to separated flow beyond these x/c locations. The resulting SPL prediction for the clean case is similar to the clean case at $\alpha = 10.53°$, but the tripped case prediction is extremely small. Since these extraction positions are too far from the TE, the predicted TE noise is non-physical even the clean case has more normal-looking result than the tripped case. Except for $\alpha = 13.58°$, the predictions by the five models are able to capture the α-trend of the measurements. The current modified model show the best agreement in both magnitude and α-trend to measurements below approximately 3000Hz.

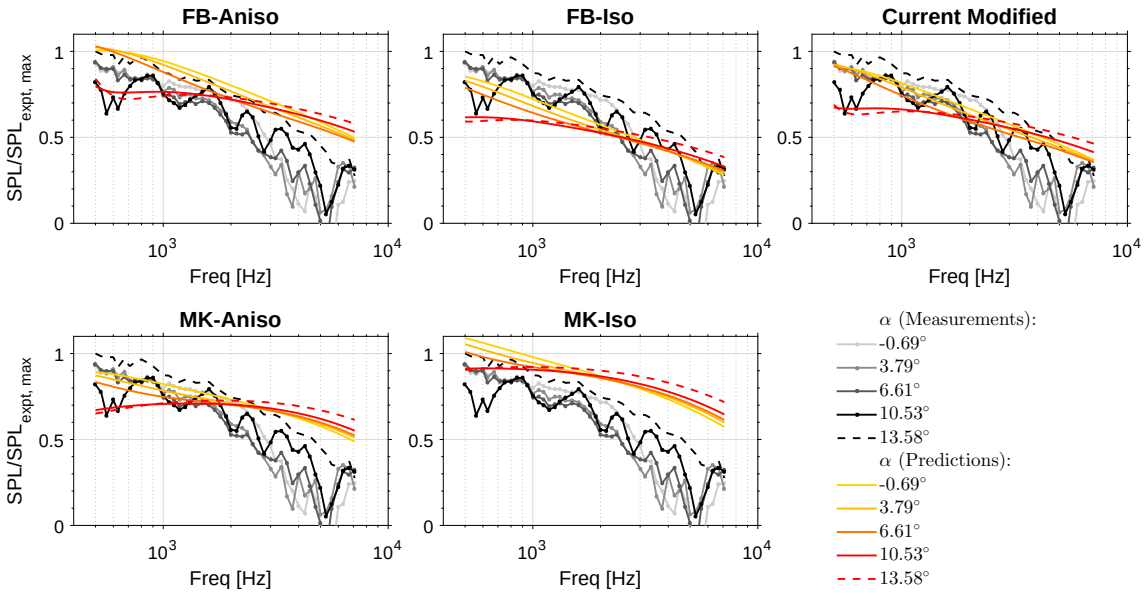

Figure 25. Case group 8.1 for a RisoB1-18 aerofoil with $U_\infty = 28$m/s and clean BL (1/12 octave)

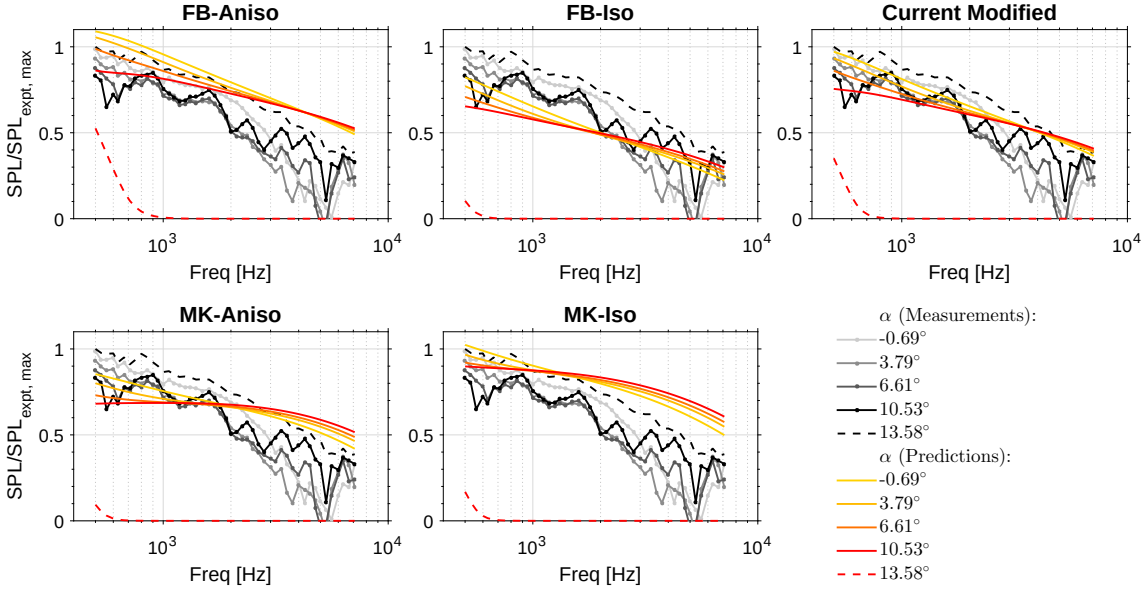

Figure 26. Case group 8.2 for a RisoB1-18 aerofoil with $U_\infty = 28$m/s and tripped BL (1/12 octave)

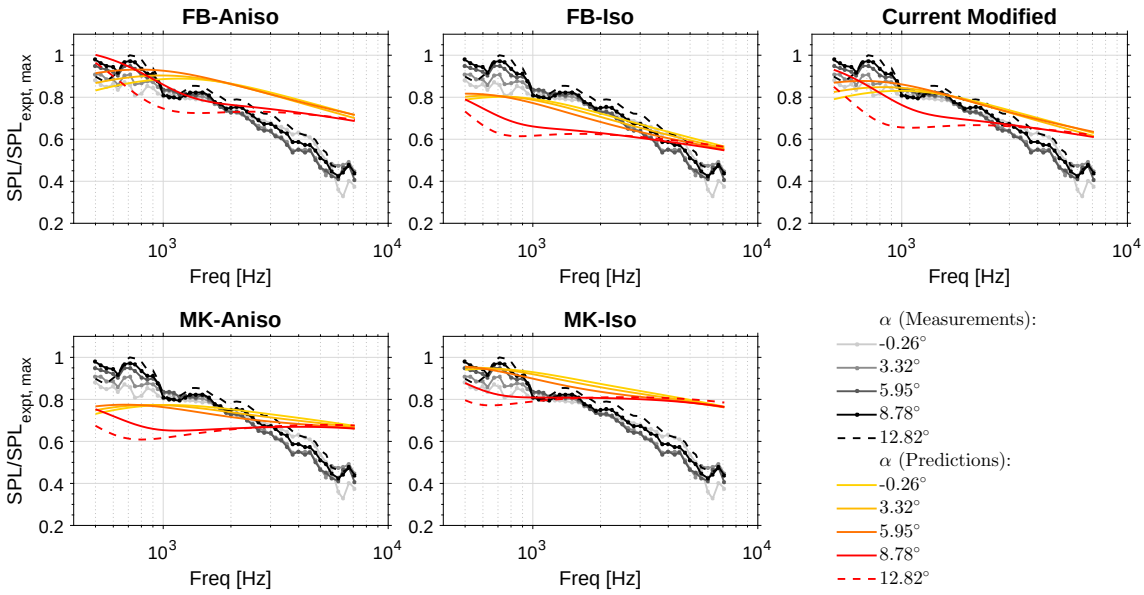

Figure 27. Case group 9.1 for a RisoB1-18 aerofoil with $U_\infty = 56$m/s and clean BL (1/12 octave)

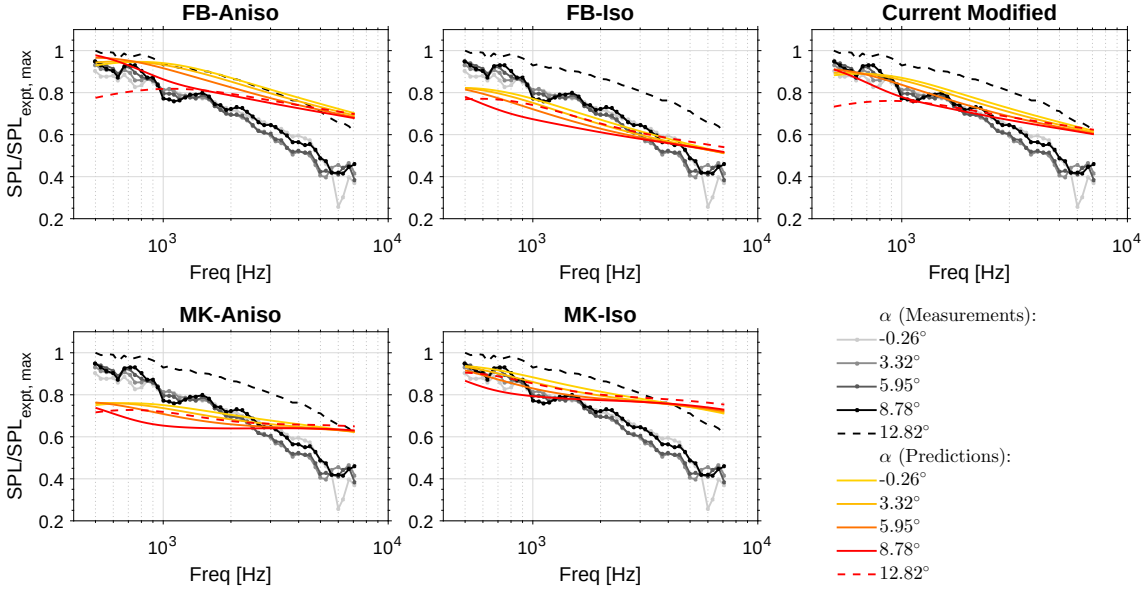

Figure 28. Case group 9.2 for a RisoB1-18 aerofoil with $U_\infty = 56$m/s and tripped BL (1/12 octave)

For the SWT measured spectra of case groups 9.1 and 9.2 for a RisoB1-18 aerofoil with U_∞ of 56m/s (Re = 3.20×10^6), increasing α leads to relatively higher SPL below approximately 1000Hz. This is similar to the LWT measurements. However, for higher frequencies, the measured SPL increases with increasing α except for a small region of about 200Hz wide above 1000Hz. One exception is the case with the lowest α of -0.26°, which shows the highest measured SPL between approximately 3000 and 5000Hz. For the tripped case group 9.2, the much higher measured SPL for $\alpha = 12.82°$ over the whole measured frequency range indicates that flow separation noise is the dominant noise source at that α. For the clean case group 9.1, the measured SPL spectrum for $\alpha = 12.82°$ still retains much of the shape and α-trend of the lower-α spectra, and is not significantly higher than the spectra at lower α. Therefore, significant flow separation has not occurred and TE noise is still the dominant noise source for that case. The current aerodynamic calculation is able to extract BL properties at $x/c = 0.994$ for both case groups 9.1 and 9.2 at all α considered. Hence TE flow separation is not predicted for both case groups. This is different to the measurements for the tripped case group 9.2. It can be seen from figures 27 and 28 that the five model predictions only show the same α-trend as the measurements at the lowest frequencies for both case groups. Similar to the measurements and predictions of the clean LWT case group 5.1 (same aerofoil with similar Re), the predicted spectra for the highest α for case group 9.1 have the lowest SPL beyond the low-frequency part. However, this trend cannot be observed from the corresponding SWT measurements. Again, the current modified and FB-Aniso TNO show the best α-trend prediction performance, particularly for the clean case group 9.1 below approximately 600 and 700Hz.

The SWT measured spectra for case group 10.1 for an clean A-18 aerofoil with U_∞ of 51.6m/s (Re = 2.95×10^6) show increased SPL with increasing α. The exception being the measured spectrum for $\alpha = -1.6°$, which has the lowest SPL up to about 2000Hz, becomes among the highest between approximately 3000 to 4000Hz and then becomes one of the lowest at higher frequencies. This α-trend is totally different to that observed for the LWT case group 6.1 for an clean A-18 aerofoil with a similar Re. All five models predict different α-trend to case group 10.1 over much of the frequency range. The current modified model shows the same α-trend as the measurements below approximately 800Hz.

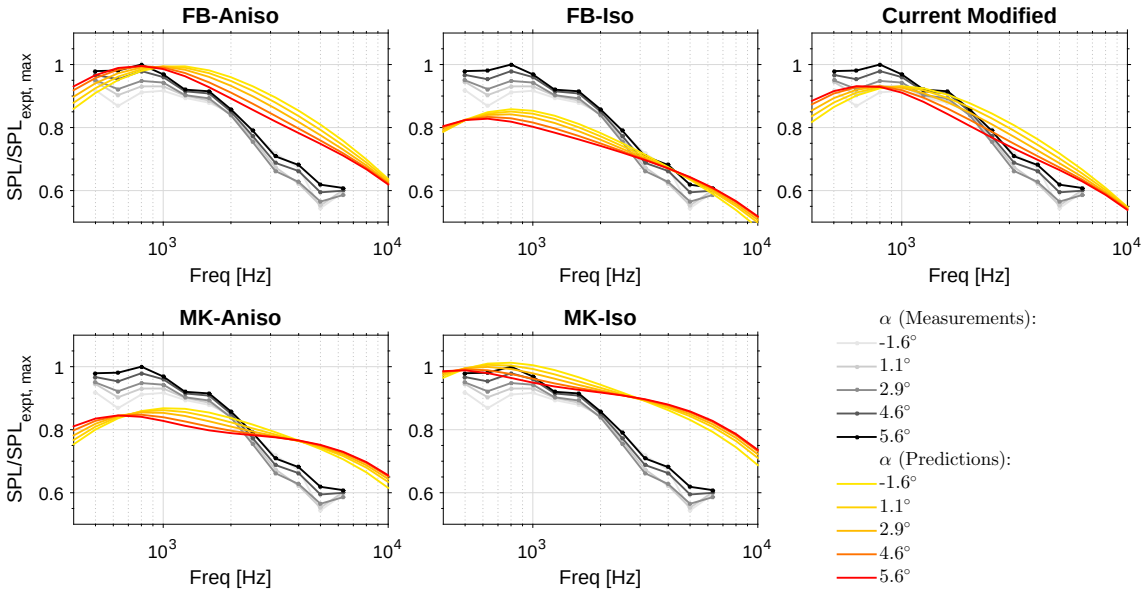

Figure 29. Case group 10.1 for an A-18 aerofoil with $U_\infty = 51.6$m/s and clean BL (1/3 octave)

This qualitative analysis shows that the α-trend of the SWT and LWT measurements are generally different, even for the same aerofoil at similar Re. The five TNO model variants tested are better in capturing the α-trend of the LWT measurements. For three out of the four cases with α higher than 12°, either significant separated flow can be deduced from the current aerodynamic and aeroacoustic results, or the code does not predict significant separated flow contrary to

experimental measurements. In general, the predictions by the current modified TNO model show the best agreement with the measurements from both wind tunnels in terms of SPL spectral shape and magnitude and α-trend.

To quantify the closeness of the predicted and the measured SPL spectra, a L^2-norm difference Δ is defined, such that

$$\Delta_k = \sqrt{\frac{1}{\log_{10}(f_b) - \log_{10}(f_a)} \int_{\log_{10}(f_a)}^{\log_{10}(f_b)} \left(\frac{\mathrm{SPL}_{\mathrm{expt},k} - \mathrm{SPL}_{\mathrm{model},k}}{\mathrm{SPL}_{\mathrm{expt},k}} \right)^2 d\log_{10}(f)},$$

where k denotes one of the test cases; f is the sound frequency; f_a and f_b are the centre-frequencies of the lower and upper frequency bands respectively; $\mathrm{SPL}_{\mathrm{expt},k}$ and $\mathrm{SPL}_{\mathrm{model},k}$ are the experimentally-measured and the model-predicted SPL respectively. The LWT and SWT test cases are considered separately. For each of the five sets of TNO model predictions, a mean Δ is defined such that

$$\Delta_{\mathrm{mean}} = \left(\frac{1}{N} \sum_{k=1}^{N} \Delta_k \right),$$

where N is the number of test cases, with $N = 40$ and 22 for the LWT and SWT comparisons respectively. Three of the 25 SWT test cases are not included ($\alpha = 13.58^\circ$ for case groups 8.1 and 8.2, and $\alpha = 12.82^\circ$ for case group 9.2) since these cases are suggested by at least one of the predictions and measurements to be dominated by flow separation noise.

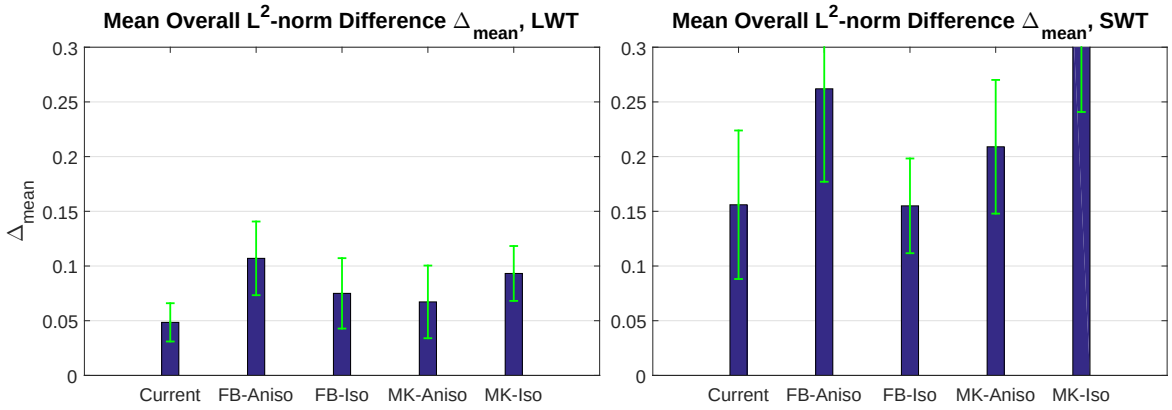

Figure 30. Δ_{mean} for the TNO model predictions compared with LWT and SWT measurements, f_b is the highest measured frequency available except for SWT case groups 8.1 and 8.2, whose $f_b = 3000$Hz

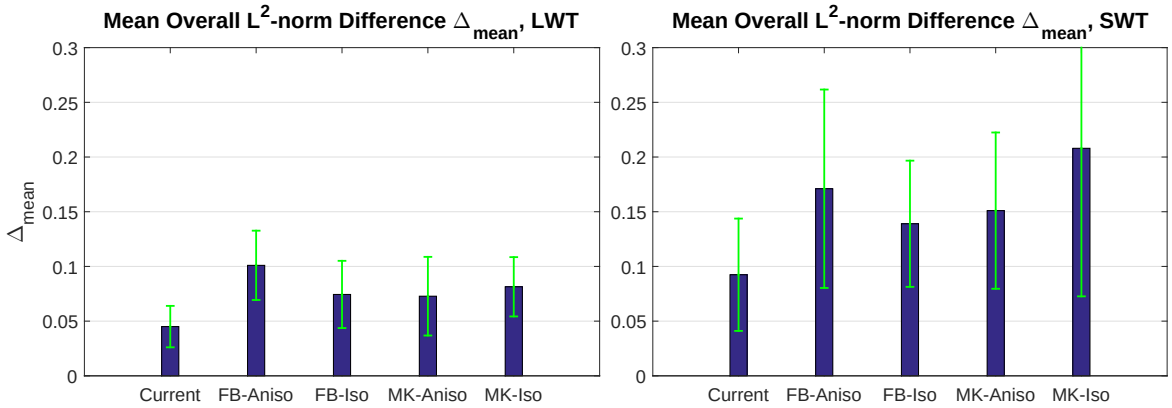

Figure 31. Δ_{mean} for the TNO model predictions compared with LWT and SWT measurements, $f_b = 3000$Hz for all cases

Figure 30 shows a set of Δ_{mean} values and the standard deviations of Δ about these Δ_{mean} for the TNO model predictions compared with LWT and SWT measurements. For this set of values, f_a and f_b for the LWT cases are

determined by the availability of the experimental data for each case, and frequency bands lower than 1000Hz are not considered due to the limits of the CPV experimental method as explained before. For most SWT cases, $f_a = 500$Hz and f_b is the highest measured frequency available. For the SWT case groups 8.1 and 8.2, due to the reduced measured data quality above approximately 3000Hz, $f_b = 3000$Hz and $f_a = 500$Hz for these two case groups. It can be seen from the figure that the current modified model has the smallest and second-smallest Δ_{mean} for the LWT and SWT comparisons respectively. For the SWT cases, the Δ_{mean} of the current modified model is only 0.001 larger than the smallest value due to FB-Iso. The standard deviations of the current modified model are the smallest and the third-smallest for the LWT and SWT comparisons respectively. The SPL spectra in figures 25 to 29 show that the predictions by FB-Iso have the closest agreement to the SWT measurements in terms of magnitude above approximately 3000Hz. This leads to the low SWT Δ_{mean} of FB-Iso although its predictions below 3000Hz are in general much further from the measurements than the current modified model, whose predictions have the second closest agreement in magnitude to the SWT measurements above 3000Hz.

Figure 31 shows another set of Δ_{mean} and standard deviation values. For this set of values, $f_b = 3000$Hz for all LWT and SWT cases, and f_a for all cases are the same as the calculation of the last set, i.e. f_a is kept at 1000Hz if available for the LWT cases, and 500Hz for the SWT cases. It can be seen that for the LWT comparisons, the Δ_{mean} and standard deviation values are similar to the last set. Hence the effect of the SPL differences between predictions and measurements above 3000Hz is small for the LWT cases. For the SWT comparisons, all models except for FB-Iso show significant reduction in Δ_{mean}. This confirms that the performance of FB-Iso depends more strongly on the agreement of its predictions to SWT measurements above 3000Hz. The current modified model has the lowest Δ_{mean} and standard deviation values for both LWT and SWT comparisons. This confirms that for frequency below approximately 3000Hz, the current modified TNO model predicts the closest SPL spectra to the measurements obtained from both LWT and SWT.

5. CONCLUSIONS

A modified TNO model is proposed by deriving new formulations for the computation of the wall pressure fluctuation spectrum. This is achieved by using the approximate ratio of the normal Reynolds stress components for an anisotropic flow over a flat plate to estimate the vertical Reynolds stress component, and by introducing new stretching factors in the streamwise, vertical and spanwise directions to take the effects of turbulent flow anisotropy into account. The suitability of the current modified model and four other TNO model variants for wind turbine aerofoil aeroacoustic design has been analysed by comparing two aspects of the numerically-predicted and the experimentally-measured SPL spectra. The first aspect is the SPL difference between two different aerofoils at similar lift coefficients within a certain frequency range (referred to as the delta noise). The second is the closeness of the predicted and measured SPL spectra of aerofoils in various flow configurations. The current comprehensive test and validation process employs experimental measurements for ten different aerofoils: seven in the delta noise analysis and seven in the SPL spectra closeness study (four aerofoils are commonly used in both analyses). Some of these aerofoils are used on modern large wind turbines. The experimental data used in the comparisons were obtained in two different wind tunnels of very different designs. The delta noise analysis is based on comparing two parameters. One of the parameters is an overall SPL difference between an aerofoil pair based on the A-weighted spectra, and the contribution of each frequency band is added by first converting the SPL to mean square pressure. The other parameter is the difference between the sums of the A-weighted SPL in dB(A) of the two aerofoils. By comparing the sign of the two delta noise parameters derived from predictions and measurements, it has been shown that the current modified model has the joint highest delta noise prediction accuracy with two other TNO model variants, one of which is the baseline of the current model. Furthermore, for the SPL spectral shape and magnitude and the changes in SPL due to increasing angle of attack, the SPL closeness study has shown that the predictions by the current model are the most consistent and closest to measurements for the vast majority of aerofoils and flow configurations tested in the

two wind tunnels, particularly for frequencies below approximately 3000Hz. Hence the current modified TNO model is suitable to be used for wind turbine aerofoil and blade aeroacoustic designs.

ACKNOWLEDGEMENT

The authors gratefully acknowledge the support of EPSRC (Engineering & Physical Sciences Research Council) KTS (Knowledge Transfer Secondment), Innovate UK KTP (Knowledge Transfer Partnership) and Vestas Technology R&D UK in the completion of this work.

REFERENCES

1. J. Ladenburg, M. Termansen, and B. Hasler, "Assessing acceptability of two onshore wind power development schemes: a test of viewshed effects and the cumulative effects of wind turbines," *Energy*, vol. 54, pp. 45–54, 2013.
2. T. Cho, C. Kim, and D. Lee, "Acoustic measurement for 12% scaled model of NREL Phase VI wind turbine by using beamforming," *Curr. Appl. Phys.*, vol. 10(2), Supplement, pp. S320–S325, 2010.
3. W. Shen and J. Sorensen, "Aero-acoustic modelling using large eddy simulation," *J. Phys. Conf. Ser.*, vol. 75, 2007.
4. A. Tadamasa and M. Zangeneh, "Numerical prediction of wind turbine noise," *Renew. Energ.*, vol. 36(7), pp. 1902–1912, 2011.
5. T. Brooks, D. Pope, and M. Marcolini, "Airfoil self-noise and prediction," tech. rep., NASA, 1989.
6. M. Lowson, "A new prediction model for wind turbine noise," in *Renewable Energy Int. Conference on Clean Power*, pp. 177–182, 1993.
7. P. Moriarty and P. Migliore, "Semi-empirical aeroacoustic noise prediction code for wind turbines," tech. rep., NREL, 2003.
8. P. Moriarty, G. Guidati, and P. Migliore, "Prediction of turbulent inflow and trailing-edge noise for wind turbines," in *11th AIAA/CEAS Aeroacoustics Conference*, 2005.
9. R. Kraichnan, "Pressure fluctuations in turbulent flow over a flat plate," *J. Acoust. Soc. Am.*, vol. 28, pp. 378–390, 1956.
10. W. Blake, *Mechanics of flow-induced sound and vibration V2: Complex flow-structure interactions*. Elsevier, 2012.
11. R. Parchen, "Progress report DRAW: a prediction scheme for trailing-edge noise based on detailed boundary-layer characteristics," Tech. Rep. TNO Rept. HAG-RPT-980023, TNO Institute of Applied Physics, 1998.
12. K. Chandiramani, "Diffraction of evanescent waves, with applications to aerodynamically scattered sound and radiation from unbaffled plates," *J. Acoust. Soc. Am.*, vol. 55, pp. 19–29, 1974.
13. T. Brooks and T. Hodgson, "Trailing edge noise prediction from measured surface pressures," *J. Sound Vib.*, vol. 78(1), pp. 69–117, 1981.
14. D. Chase, "Sound radiated by turbulent flow off a rigid half-plane as obtained from a wavevector spectrum of hydrodynamic pressure," *J. Acoust. Soc. Am.*, vol. 52, pp. 1011–1023, 1972.
15. R. Amiet, "Noise due to turbulent flow past a trailing edge," *J. Sound Vib.*, vol. 47(3), pp. 387–393, 1976.
16. R. Amiet, "Effect of the incident surface pressure field on noise ude to turbulent flow past a trailing edge," *J. Sound Vib.*, vol. 57(2), pp. 305–306, 1978.
17. M. Roger and S. Moreau, "Back-scattering correction and further extensions of amiet's trailing-edge noise model. part 1: theory," *J. Sound Vib.*, vol. 286(3), pp. 477–506, 2005.
18. T. Lutz, A. Herrig, W. Wurz, M. Kamruzzaman, and E. Kramer, "Design and wind-turbine verification of low-noise airfoils for wind turbines," *AIAA J.*, vol. 45(4), pp. 779–785, 2007.

19. M. Kamruzzaman, D. Bekiropoulos, A. Wolf, T. Lutz, and E. Kramer, “Rnoise: a RANS based airfoil trailing-edge noise prediction model,” in *20th AIAA/CEAS Aeroacoustics Conference Proc.*, 2014.
20. F. Bertagnolio, A. Fischer, and W. Zhu, “Tuning of turbulent boundary layer anisotropy for improved surface pressure and trailing-edge noise modeling,” *J. Sound Vib.*, vol. 333(3), pp. 991–1010, 2014.
21. D. Wilcox, *Turbulence modeling for CFD*. DCW Industries, Inc., second ed., 2000.
22. M. Drela, *Low Reynolds number aerodynamics*. Springer Berlin Heidelberg, 1989.
23. O. Stalnov, P. Chaitanya, and P. Joseph, “Prediction of broadband trailing-edge noise based on Blake model and Amiet theory,” in *21st AIAA/CEAS Aeroacoustics Conference*, 2015.
24. P. Lysak and T. Brungart, “Velocity spectrum model for turbulence ingestion noise from computational-fluid-dynamics calculations,” *AIAA J. Technical Notes*, vol. 41(9), pp. 1827–1829, 2003.
25. M. Herr and M. Kamruzzaman, “Benchmarking of trailing-edge noise computations - outcome of the BANC-II Workshop,” in *19th AIAA/CEAS Aeroacoustics Conference Proc.*, 2013.
26. A. Herrig, W. Wurz, E. Kramer, and S. Wagner, “New CPV-results of NACA 0012 trailing-edge noise,” in *International Conference of Methods of Aerophysical Research*, 2008.
27. B. Plogmann and W. Wurz, “Aeroacoustic measurements on a NACA 0012 applying the coherent particle velocity method,” *Exp. Fluids*, vol. 54(7), 2013.
28. W. Devenport, R. Burdisso, A. Borgoltz, P. Ravetta, and M. Barone, “Aerodynamic and acoustic corrections for a kevlar-walled anechoic wind tunnel,” in *16th AIAA/CEAS Aeroacoustics Conference Proc.*, 2010.
29. J. Hurault, A. Gupta, E. Sloth, N. Nielsen, A. Borgoltz, and P. Ravetta, “Aeroacoustic wind tunnel experiment for serration design optimisation and its application to a wind turbine rotor,” in *6th International Meeting on Wind Turbine Noise*, 2015.